Supporting Information

-for-

Levitation-guided disorder engineering unlocks efficient nitrite-to-ammonia electroconversion

Juhyeon Park,[†a] Jayesh Cherusseri,[†a] Jayaraman Theerthagiri,[†a] Ahreum Min[†a] Anuj Kumar,[†b] Gyeong-Ah Kim,[c] Nivarthi Rajiv Bharadwaj,[a] Sanggyeong Lee,[a] Rimal Isaac R.S[d] and Myong Yong Choi*[ac]

[a] Department of Chemistry (BK21 FOUR), Research Institute of Advanced Chemistry, Gyeongsang National University, Jinju 52828, Republic of Korea

[b] Nano-Technology Research Laboratory, Department of Chemistry, GLA University, Mathura, Uttar Pradesh 281406, India

[c] Core-Facility Center for Photochemistry & Nanomaterials, Gyeongsang National University, Jinju 52828, Republic of Korea

[d] Department of Nanotechnology, Noorul Islam Centre for Higher Education, Kumaracoil, Thuckalay, Kanyakumari, Tamil Nadu 629180, India

* Corresponding author E-mail: mychoi@gnu.ac.kr (M. Y. Choi)

† These authors contributed equally to this work

Method S1. Material Characterizations

The crystal structures of the materials were characterized by X-ray diffraction (XRD, Bruker D8 Advance A25, Germany) using Cu-Kα radiation (λ = 1.542 Å). Raman spectroscopy was performed using a DXR 2xi Raman microscope (Thermo Fisher Scientific, USA) equipped with a continuous-wave laser operating at a wavelength of 532 nm. The microstructure and surface morphology were examined using field-emission scanning electron microscopy (FESEM, TESCAN S8000, Czech Republic). Elemental composition and spatial distribution were analyzed via energy-dispersive X-ray spectroscopy (EDS, Ultim Max, Oxford Instruments), integrated with the FESEM system. High-resolution transmission electron microscopy (HRTEM, FEI Tecnai TF30ST, USA) was conducted at an accelerating voltage of 300 kV to observe the ultrafine structural features. Fourier transform infrared (FTIR) spectroscopy (Nicolet iS10, Thermo Fisher Scientific, USA) was employed to investigate the chemical bonding. Surface chemical states were further analyzed using X-ray photoelectron spectroscopy (XPS, NEXSA G2, Thermo Fisher Scientific, USA) with monochromatic Al–K*α* radiation.

Method S2. Preparation of Catalyst Electrodes

Catalyst electrodes for electrochemical measurements were prepared by depositing the catalyst material onto a carbon cloth substrate. In a typical procedure, a homogeneous catalyst ink was prepared by sonicating a slurry containing 1 mg of catalyst, 95 μL of deionized water, 95 μL of ethanol, and 10 μL of Nafion solution (5 wt%) for 30 min. The resulting ink was then drop-cast onto a pre-cleaned carbon cloth substrate with a geometric area of 1 cm × 1 cm and subsequently dried at 60 °C for 3 h.

Method S3. Electrochemical Measurements

All electrochemical measurements for eNO_2RR were conducted using a CHI 708E electrochemical workstation (CH Instruments, USA) in a two-compartment H-type cell. The working electrode consisted of the catalyst coated onto carbon cloth (CC) via a slurry-casting method. A platinum wire and a Hg/HgO electrode were used as the counter and reference electrodes, respectively. The catholyte consisted of 0.1 M KNO_2 in 1 M KOH, while 1 M KOH was used as the anolyte. The anodic and cathodic compartments were separated by a pretreated Nafion-117 membrane. The membrane was sequentially soaked in 3% H_2O_2 for 1 h, deionized water for 2 h, and 0.5 M H_2SO_4 for 1 h at 80°C, followed by repeated washing with deionized water. For electrode preparation, a homogeneous slurry was prepared by sonicating 1 mg of catalyst in a mixture of 95 μL of deionized water, 95 μL of ethanol, and 10 μL of 5 wt% Nafion binder for 30 min. The slurry was then drop-cast onto a pretreated CC (geometric area = 1 cm^2) and dried at 60°C for 3 h. All potentials measured with respect to the Hg/HgO reference electrode were converted to the reversible hydrogen electrode (RHE) scale using the Nernst equation (1):

$$E_{RHE} = E_{Hg/HgO} + E^{0}_{Hg/HgO} + 0.059\ V \times pH \tag{1}$$

where $E_{Hg/HgO}$ is the measured potential from the Hg/HgO electrode, $E^{0}_{Hg/HgO}$ is the standard electrode potential (0.098 V), and pH is the electrolyte pH.

Tafel slopes were calculated from the polarization curves by plotting the overpotential (η) versus the logarithm of the current density (j). The Tafel slope was determined using the following equation (2):

$$\eta = a + (b \times \log(j)) \tag{2}$$

where b represents the Tafel slope, and a denotes the Tafel constant.

Electrochemical impedance spectroscopy (EIS) analysis was performed at a fixed potential

(V vs. RHE) within a frequency range of 0.1 - 10^5 Hz. The turnover frequency (TOF) of the electrocatalysts was calculated using the following equation (3):

$$\text{TOF }(\text{s}^{-1}) = \frac{j\ x\ N_A}{n\ x\ F\ x\ S_a} \tag{3}$$

Where, N_A is the Avogadro's number, n is the number of electrons involved during the reaction, F is the Faraday constant (96,485.3 C mol^{-1}), and S_a is the number of available active sites. The active sites (S_a) can be determined using the following equation (4):

$$S_a = \frac{(\int Area\ under\ the\ reduction\ curve/Scan\ rate)}{Charge\ of\ the\ electron} \tag{4}$$

The electrochemical double-layer capacitance (C_{dl}) was estimated from cyclic voltammetry (CV) measurements by plotting the average current density difference ($\Delta j/2 = (j_a - j_c)/2$) versus the scan rate. The slope of the resulting linear plot represents the electrochemical C_{dl} of the material, which was calculated using the equation (5):

$$C_{dl} = \frac{d(\Delta j)}{2dv} \tag{5}$$

Where, ν represents the scan rate.

Method S4. Quantification of NH_4^+ Product

The yield of NH_4^+ produced after eNO_2RR electrolysis for 1 was quantified using the colorimetric indophenol blue method. After NO_2^- electroreduction, 50 µL of catholyte was extracted from the electrolytic cell and mixed with 2 mL of 1 M NaOH solution containing 5 wt.% sodium citrate dihydrate and 5 wt.% salicylic acid. Subsequently, 1 mL of NaClO (0.05 M) and

0.2 mL of sodium nitroferricyanide (0.1 wt.%) were added to the mixture, which was then allowed to stand in the dark for 2 h. Following this, UV-visible spectra (Thermo Fisher Scientific, USA) Thermo Scientific were recorded at ~655 nm, and NH_4^+ concentrations were quantified using a calibration curve based on NH_4Cl standards (5, 10, 50, 100, 200, and 400 ppm). The NH_4^+ quantification was further confirmed via ^1H nuclear magnetic resonance spectroscopy (300 MHz, Bruker Avance-III, Germany). After 1 h of eNO_2RR, 1 mL of catholyte was mixed with 0.5 mL of D_2O and adjusted to pH 2 with 0.5 M H_2SO_4. Spectra revealed three characteristic peaks for NH_4^+. The NH_4^+ concentration was determined using a calibration curve prepared from NH_4Cl standards (100, 200, and 500 ppm).

Method S5. Calculation of NH_4^+ Yield Rate and Faradaic Efficiency

The NH_3 yield rate during eNO_2RR was calculated using the following equation (6):

$$\text{Yield rate} = \frac{C_{(N-NH_4^+)} \times V_{catholyte}}{t \times m_{cat}} \tag{6}$$

Where, $C_{(N-NH_4^+)}$ is the N concentration in the NH_4^+ (ppm, equivalent to $mg \cdot L^{-1}$), $V_{catholyte}$ is the total volume of the electrolyte in the cathode compartment (20 mL), t is the duration of the bulk electrolysis test for eNO_2RR (in hours) and m_{cat} is the catalyst loading (which can alternatively be replaced by the area of electrode). Furthermore, the NH_3 Faradaic efficiency for NH_4^+ formation was calculated using the following equation (7):

$$\text{Faradaic efficiency} = \frac{nF \times C_{(N-NH_4^+)} \times V_{catholyte}}{M_{(NH_4^+)} \times Q} \tag{7}$$

Where, $M_{(NH_4^+)}$ is the molar mass of NH_4^+ ($g \cdot mol^{-1}$), F is the Faradaic constant (96,485.3 $C \cdot mol^{-1}$), Q is the total charge passed during the reaction (C); n is the number of electrons involved in eNO_2RR ($n = 6$).

Method S6. Quantification of N_2 and H_2

N_2 and H_2 generated during eNO_2RR over CuCoPBA and CuCoPBA-S were quantified separately using gas chromatography (GC). He and N_2 were employed as carrier gases for the analysis of N_2 and H_2, respectively. The gases were quantified from calibration curves obtained by injecting known volumes (50, 100, 150, 200, and 250 μL) of the corresponding gases. Gas quantification was performed using a sealed H-type cell. Before each bulk electrolysis experiment, the cell was purged with He for 30 mins. After electrolysis, fixed volumes of the cathodic headspace gas were withdrawn using a gas-tight syringe and injected into the GC for analysis. Background measurements were conducted after He purging, before starting the bulk electrolysis experiment.

Method S7. Calculation of H_2 Yield Rate and Faradaic Efficiency

The Faradaic efficiency of H_2 was calculated using the equation:

$$Faradaic\ Efficiency = \frac{N \times n \times F}{Q} \tag{8}$$

Where, N denotes the number of moles of specific product, n is the number of electrons transferred per mole (n = 2 for H_2), F is the Faraday constant (96,485 C mol^{-1}), and Q represents the total charge passed during electrolysis.

Method S8. *In situ* Raman Spectroscopic Measurements

In situ Raman spectroscopy was performed using an electrochemical flow cell (Redoxme AB, Sweden) configured with a three-electrode setup: a catalyst-coated CC as the working electrode, a platinum wire as the counter electrode, and a Hg/HgO reference electrode. The eNO_2RR measurements were conducted in 1 M KOH containing 0.1 M KNO_2. Raman spectra were recorded at various applied potentials using a DXR3 Raman microscope (Thermo Fisher Scientific, UK) equipped with a 532 nm Nd:YAG laser and a 50X objective lens. All electrochemical operations were controlled via a CHI 708E electrochemical workstation.

Method S9. Density Functional Theory (DFT) Calculations

(a) Structural Optimization:

The optimization process for all structures was completed when the force on any atom was reduced to below 10^{-4} Ry/Bohr. To characterize the van der Waals (vdW) interactions in the CoCuPBA-S heterostructure, Grimme's semi-empirical DFT-D3 dispersion correction approach was applied. Convergence thresholds of 0.03 eV/Å for atomic forces and 10^{-5} Ry for energy were used using structural optimizations. The Brillouin zone sampling was conducted using a k-point grid of 8×10×6 generated by the Monkhorst-Pack scheme, ensuring sufficient accuracy for total energy estimations. After convergence testing, a plane-wave cutoff of 250 Ry and a charge density cutoff of 460 Ry were selected.

Spin-polarized calculations were conducted to investigate the density of states. To understand the contributions of specific atomic orbitals to the electronic structure, the projected DOS was further analyzed. Charge density maps were produced to examine the electronic distribution within the material, highlighting how structural symmetry affects electronic properties. The charge density difference was calculated using the following formula:

$$\Delta\rho_{(Density\ Differenceover\ CoCuPBA-S)} = \rho_{(CoCuPBA-S)} - \rho_{(CoCuPBA)} - \rho_{(Cu2S)} - \rho_{(Co9S8)} \quad (9)$$

(b) Gibbs Free Energy Calculations:

The catalytic activity of these high-entropy materials was evaluated by computing the Gibbs free energy (ΔG) for the NO_2 reduction process based on adsorption energies. The adsorption energies for important intermediates were determined using the equation:

$$E_{ads}=E_{slab+adsorbate}-E_{slab}-E_{adsorbate} \quad (10)$$

where $E_{slab+adsorbate}$ represents the total energy of the adsorbed system, E_{slab} is the energy of the clean surface, and $E_{adsorbate}$ is the energy of the gas-phase adsorbate. The Gibbs energy change was calculated using the following equation:

$$\Delta G = \Delta Eads + \Delta ZPE - T\Delta S + eU \quad (11)$$

Here, the symbols ΔE, ΔZPE, TΔS, and U denote the following terms: ΔE represents the variation in electronic energy; ΔZPE denotes the difference between zero-point energy and the applied electrode potential; TΔS pertains to the entropy at 273.15 K; and U symbolizes potential energy.

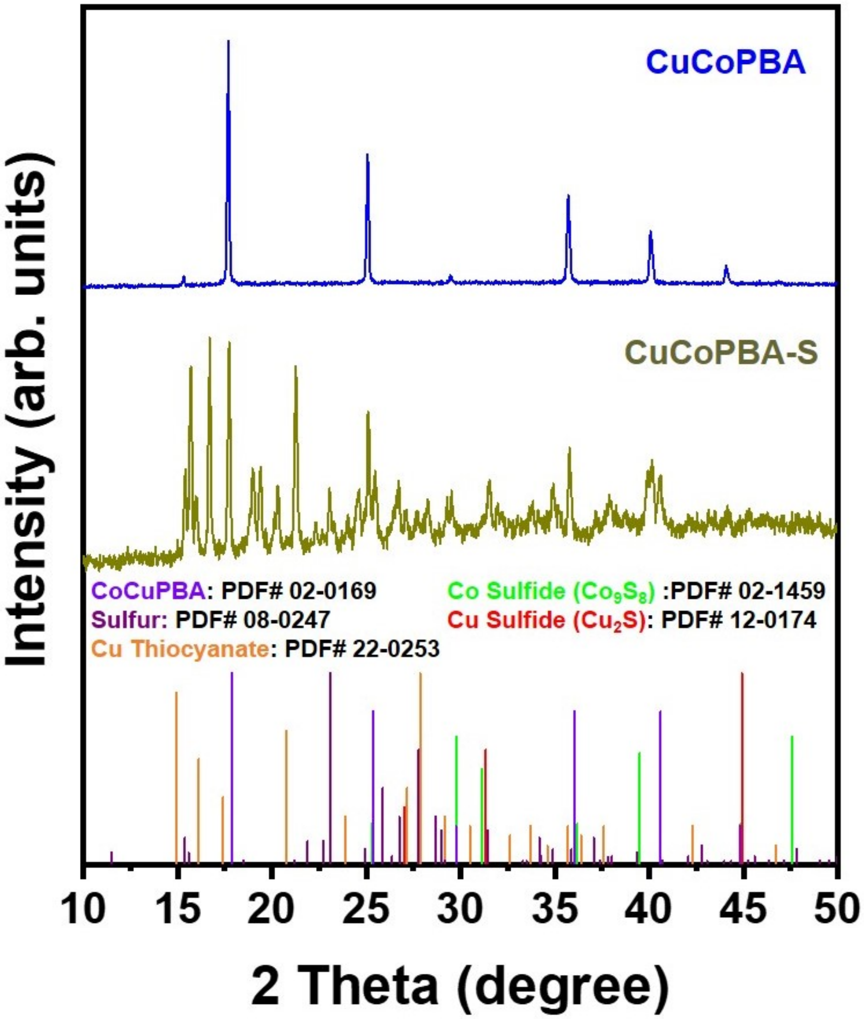

Fig. S1. XRD spectra of CoCuPBA and CoCuPBA-S.

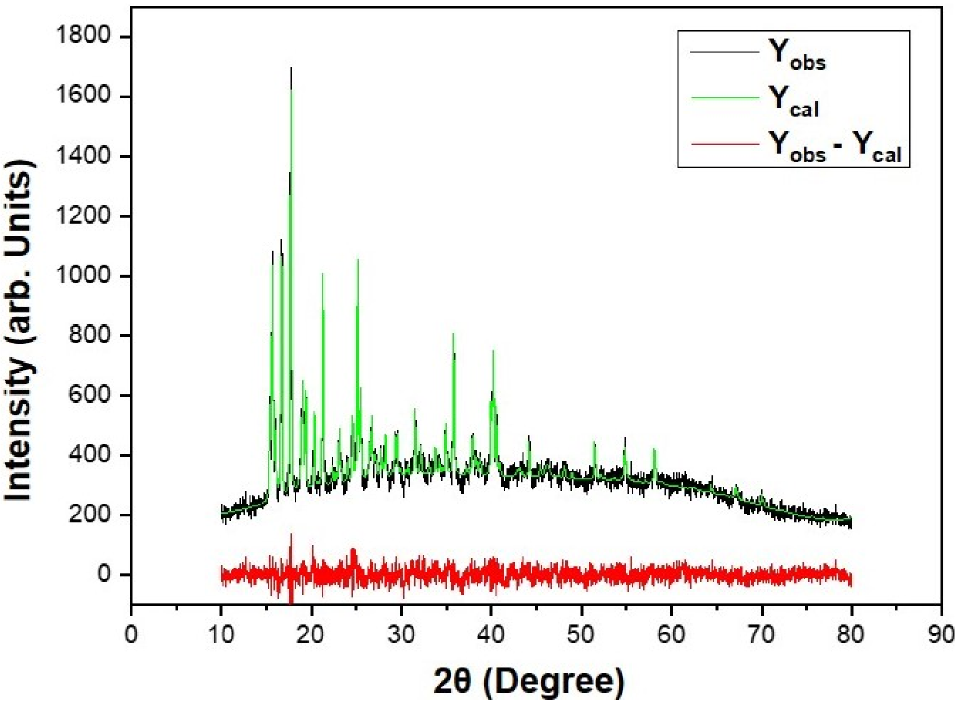

Fig. S2. XRD Rietveld analysis of CoCuPBA-S.

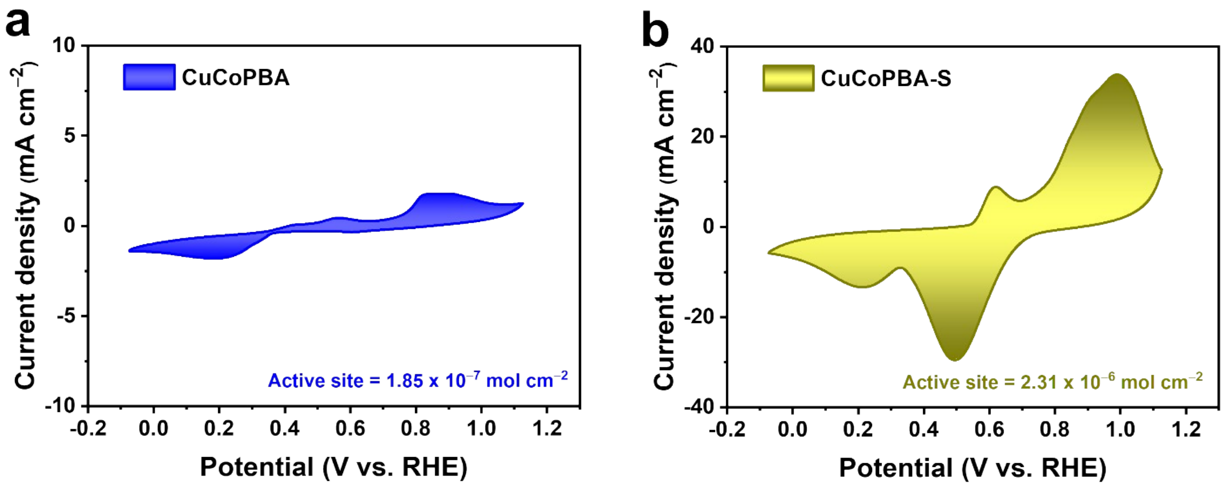

Fig. S3. CV curves of (a) CuCoPBA and (b) CuCoPBA-S electrocatalysts during the eNO$_2$RR within a potential range of −0.1 to 1.1 V vs. RHE at 50 mV s^{-1} in 1 M KOH electrolyte.

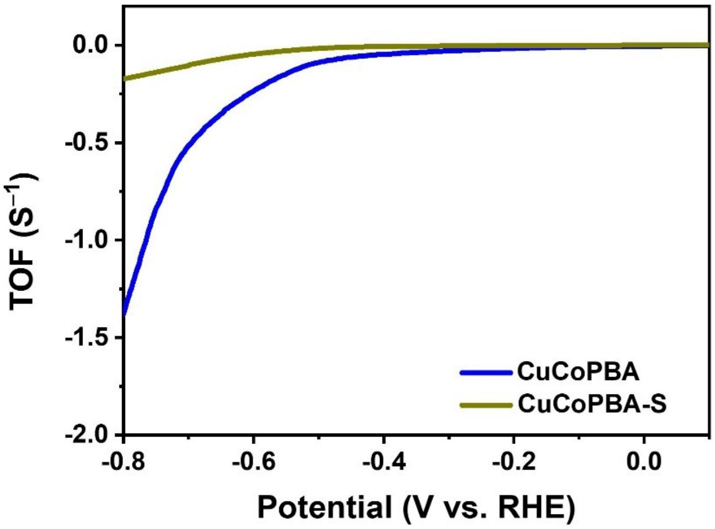

Fig. S4. TOF calculated for the CuCoPBA and CuCoPBA-S within a potential range of 0.0 to −0.8 V vs. RHE at 50 mV s^{-1} in 1 M KOH electrolyte.

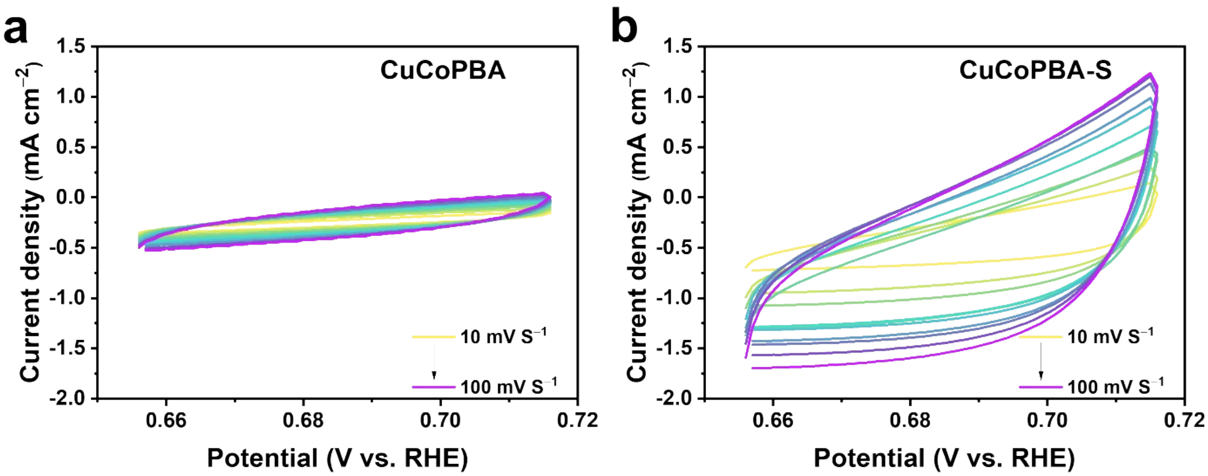

Fig. S5. CV curves of the (a) CuCoPBA and (b) CuCoPBA-S catalysts measured in the non-Faradaic potential region at various scan rates in 1 M KOH electrolyte to calculate the C_{dl}.

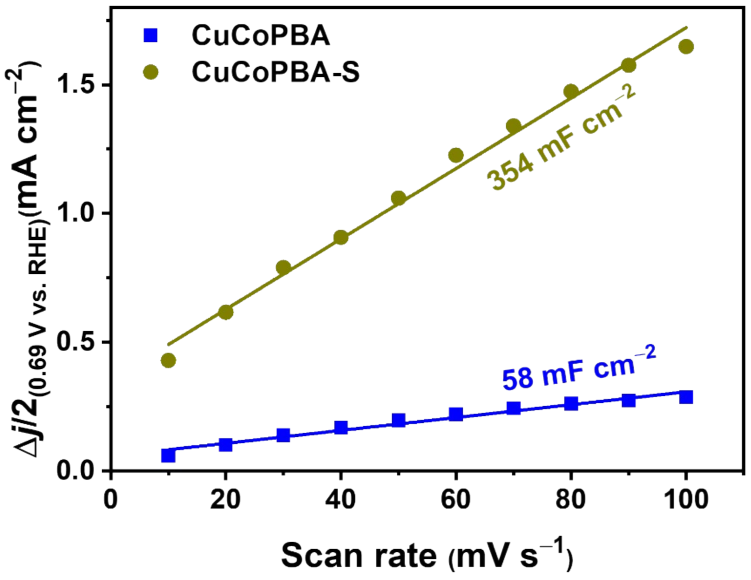

Fig. S6. The plots of Δj/2 at 0.45 V vs. RHE versus the scan rates for CuCoPBA and CuCoPBA-S catalysts with their C_{dl} values.

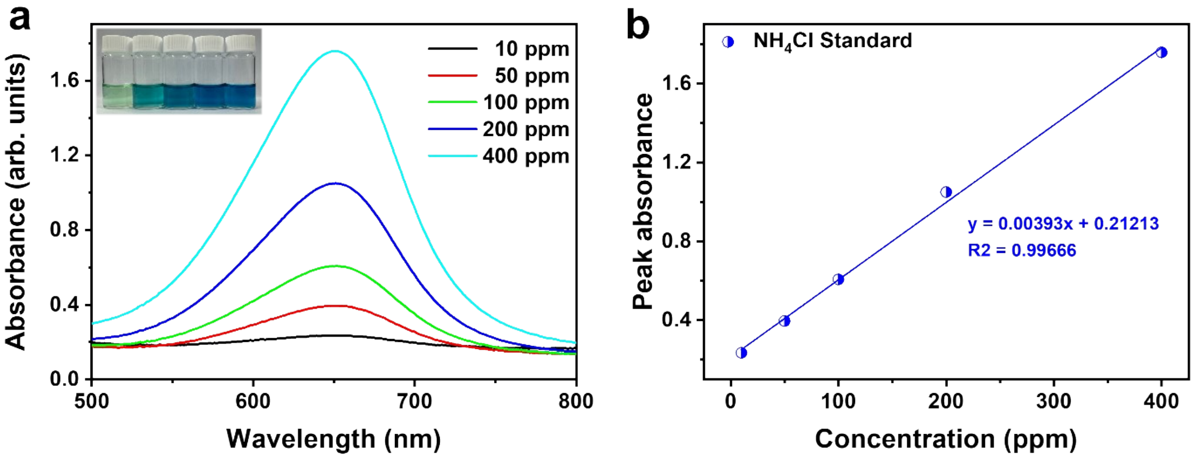

Fig. S7. (a) UV-visible absorption spectra for the NH_4Cl standard at different ppm and (b) the corresponding calibration curve.

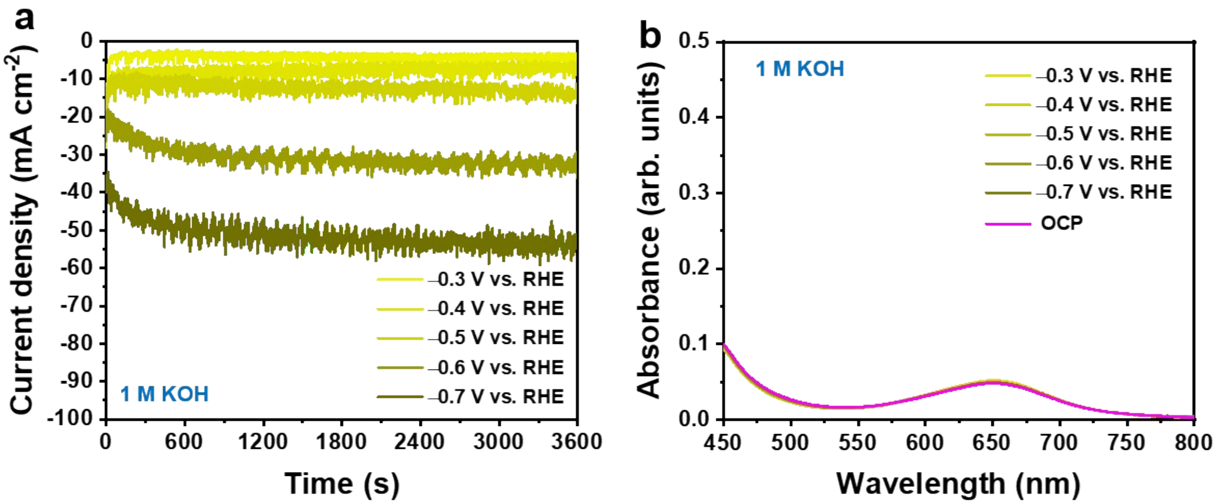

Fig. S8. (a) Variation in the current density profiles and (b) UV-Vis absorption spectra obtained during the electrolysis conducted in 1 M KOH aqueous solution at different reduction potentials.

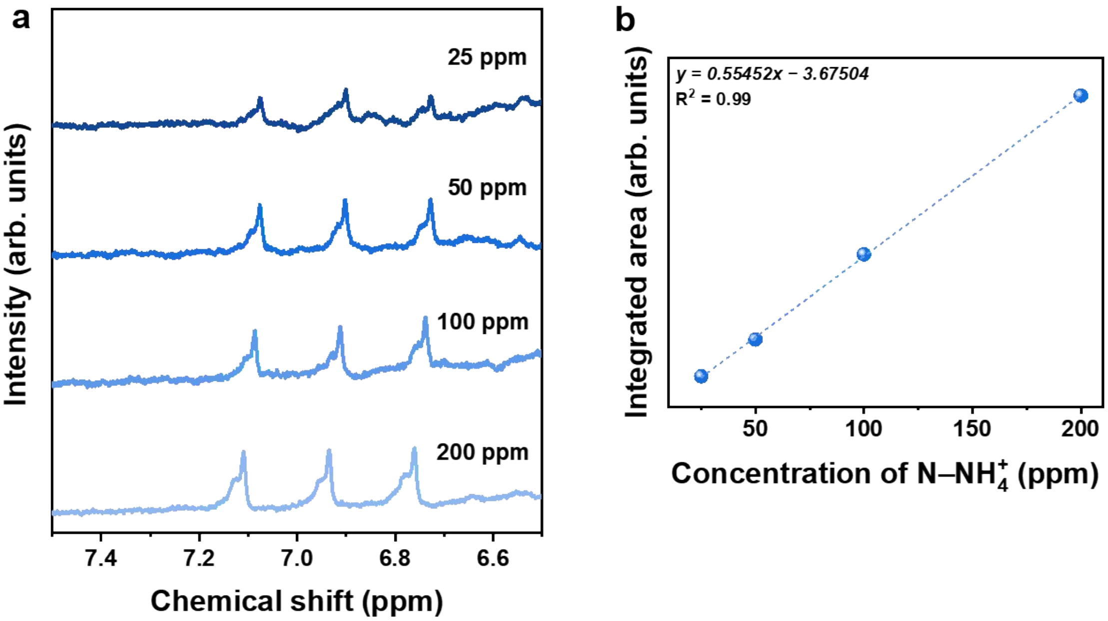

Fig. S9. (a) ^{1}H NMR spectra and (b) calibration graph used for the quantification of NH_3.

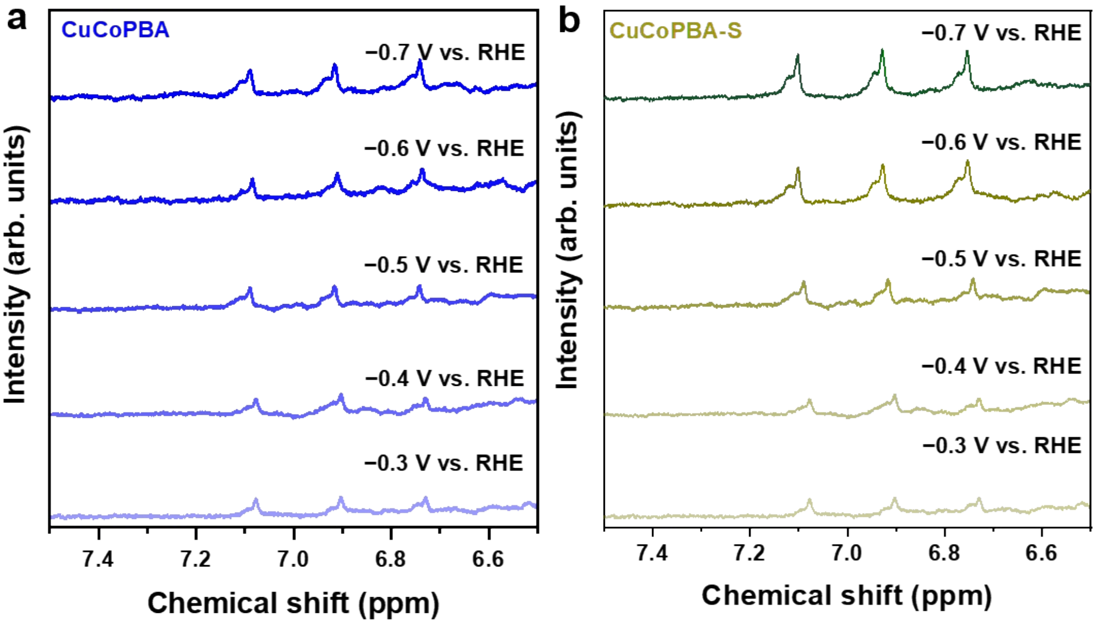

Fig. S10. ^{1}H NMR spectra obtained for the (a) CuCoPBA and (b) CuCoPBA-S at different reduction potentials for the quantification of NH_3.

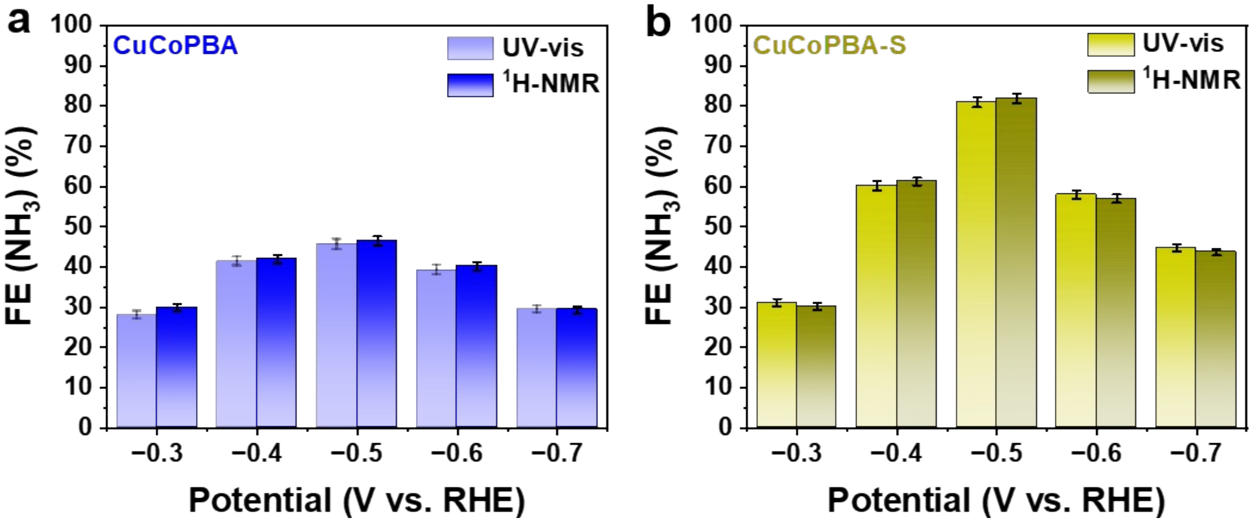

Fig. S11. Comparison of the FE (NH_3) calculated from the UV-Vis spectra and ^1H NMR spectra for the (a) CuCoPBA and (b) CuCoPBA-S at different reduction potentials.

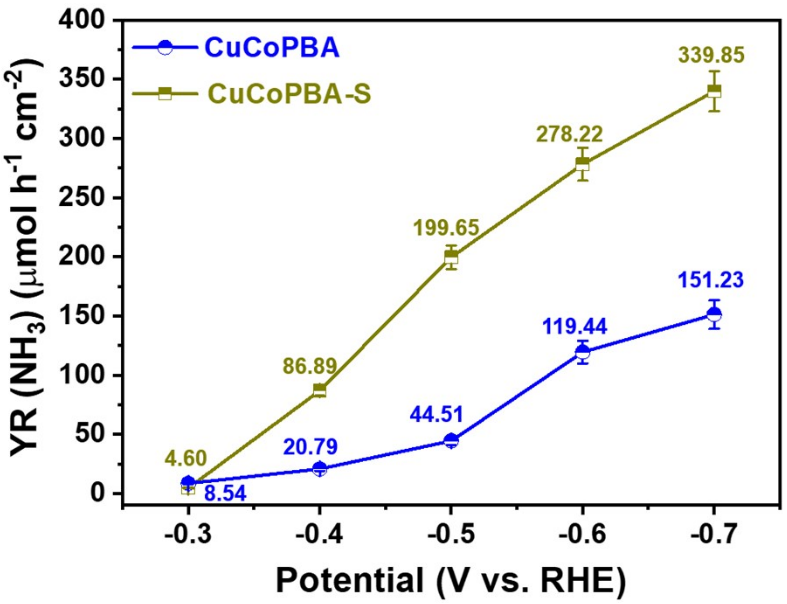

Fig. S12. YR (NH_3) calculated from the UV-vis spectra for the CuCoPBA and CuCoPBA-S at different reduction potentials expressed in units of μmol h^{-1} cm^{-2}.

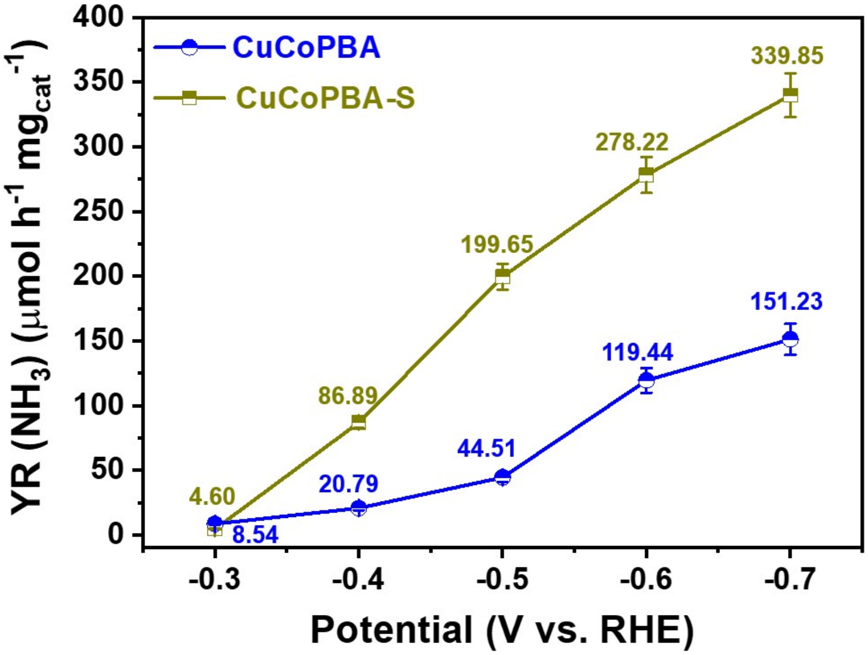

Fig. S13. YR (NH_3) calculated from the UV-vis spectra for the CuCoPBA and CuCoPBA-S at different reduction potentials expressed in units of μmol h^{-1} mg_{cat}^{-1}.

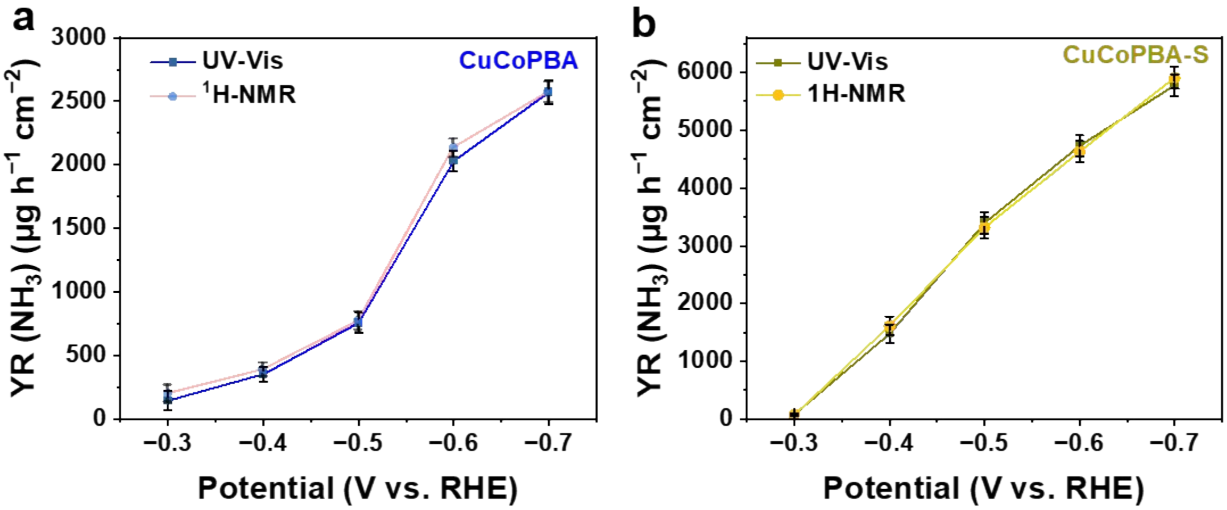

Fig. S14. Comparison of the YR (NH$_3$) in µg h^{-1} cm^{-2} calculated from the UV-vis spectra and ^{1}H NMR spectra for the (a) CuCoPBA and (b) CuCoPBA-S at different reduction potentials.

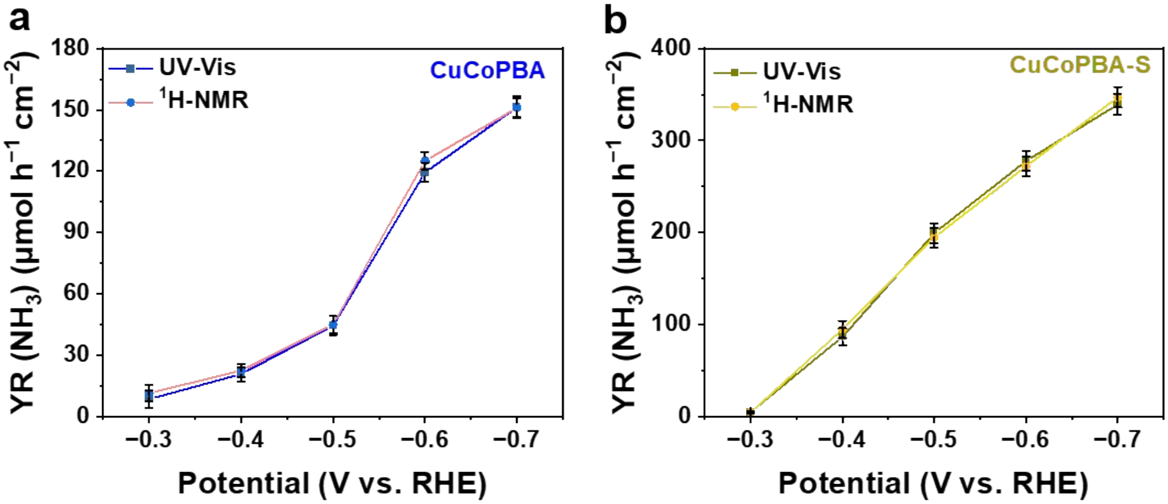

Fig. S15. Comparison of the YR (NH_3) in µmol h^{-1} cm^{-2} calculated from the UV-vis spectra and ^{1}H NMR spectra for the (a) CuCoPBA and (b) CuCoPBA-S at different reduction potentials.

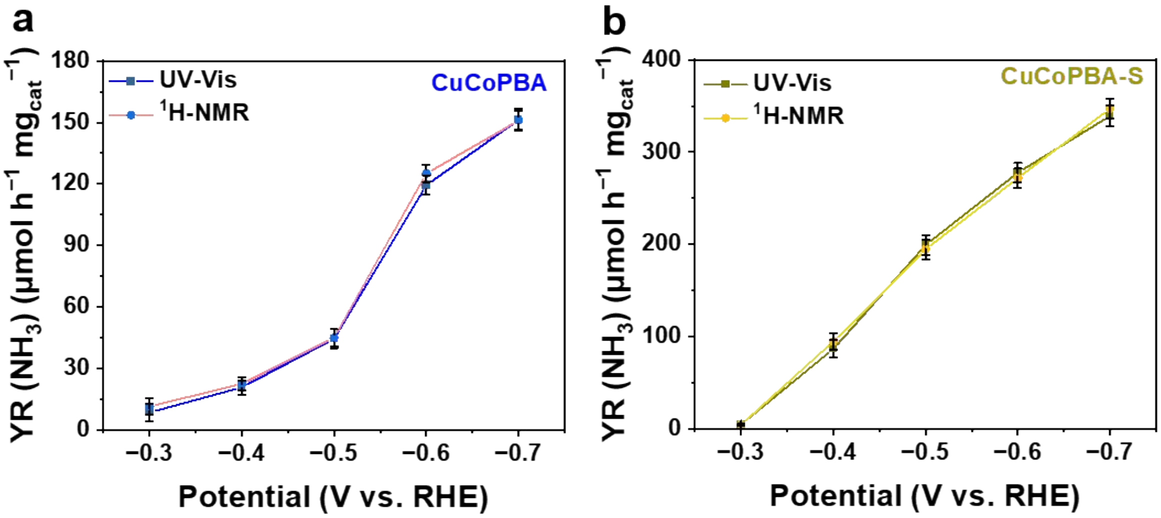

Fig. S16. Comparison of the YR (NH_3) in μmol h^{-1} mg_{cat}^{-1} calculated from the UV-vis spectra and ^1H NMR spectra for the (a) CuCoPBA and (b) CuCoPBA-S at different reduction potentials.

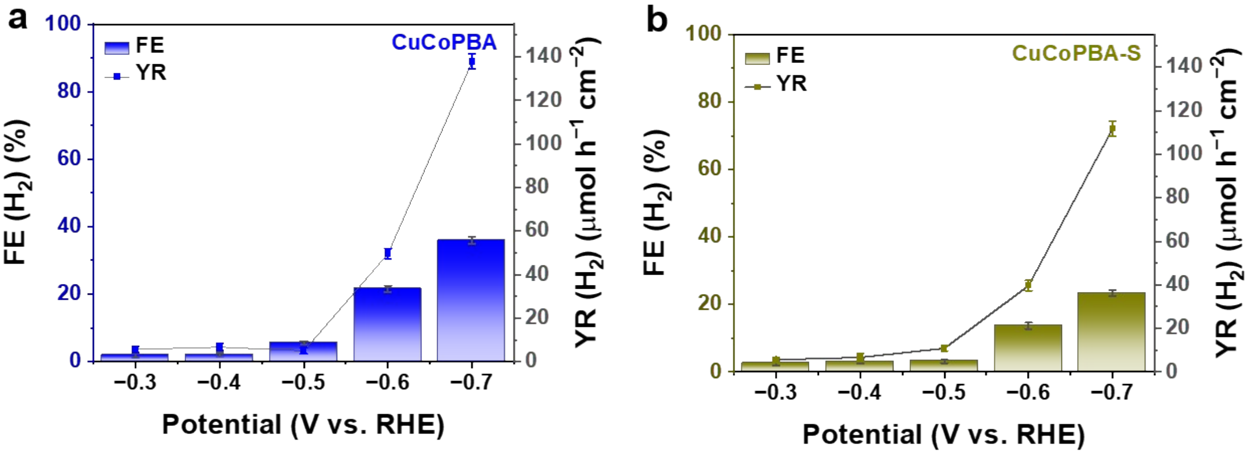

Fig. S17. Comparison of the FE (H_2) and YR (H_2) in µmol h^{-1} cm^{-2} calculated for the (a) CuCoPBA and (b) CuCoPBA-S at different reduction potentials.

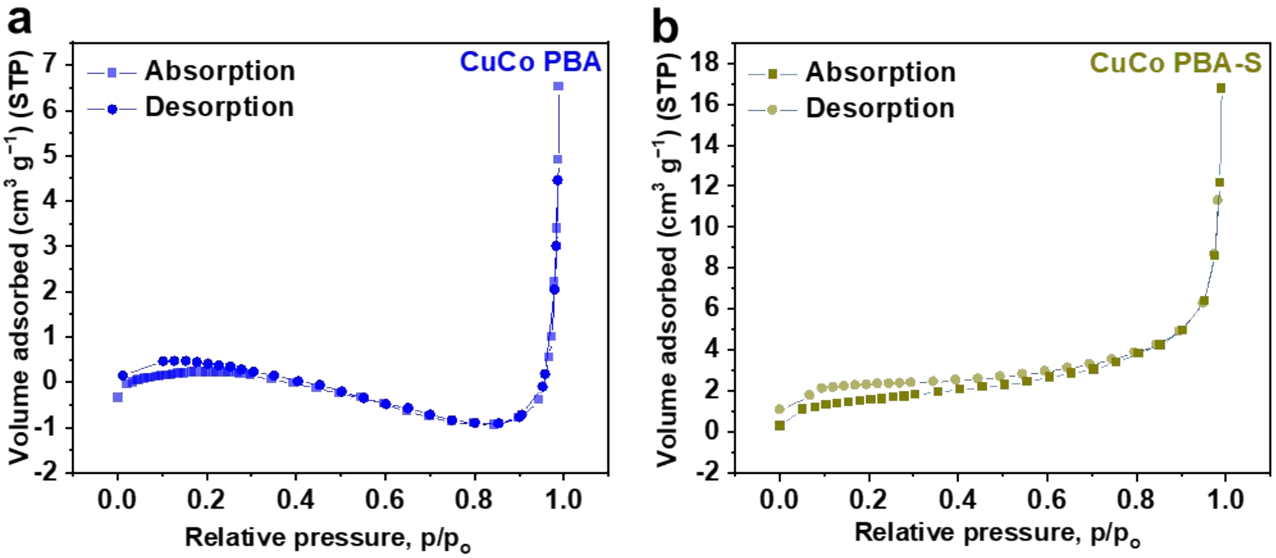

Fig. S18. N_2-sorption isotherms of (a) CuCoPBA and (b) CuCoPBA-S.

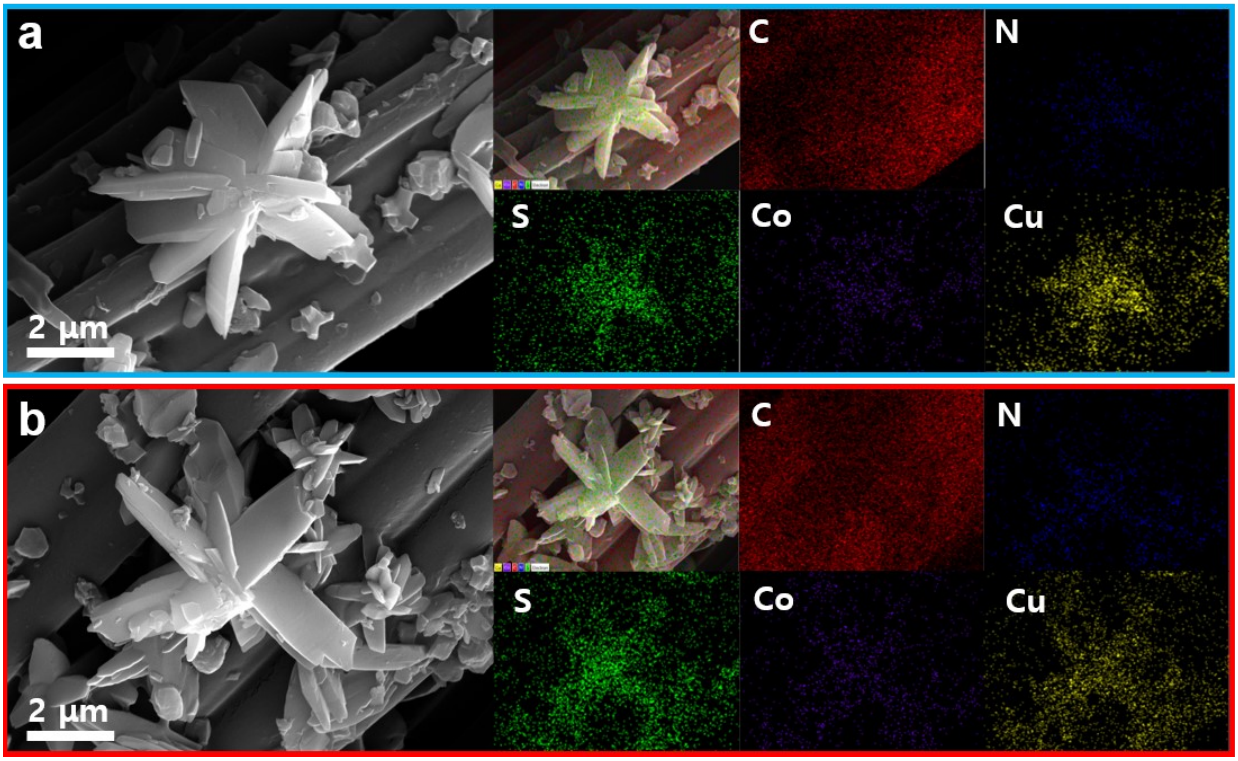

Fig. S19. FESEM images and SEM-EDS elemental mapping images for CuCoPBA-S catalyst electrode (a) before and (b) after the 10-hour stability test.

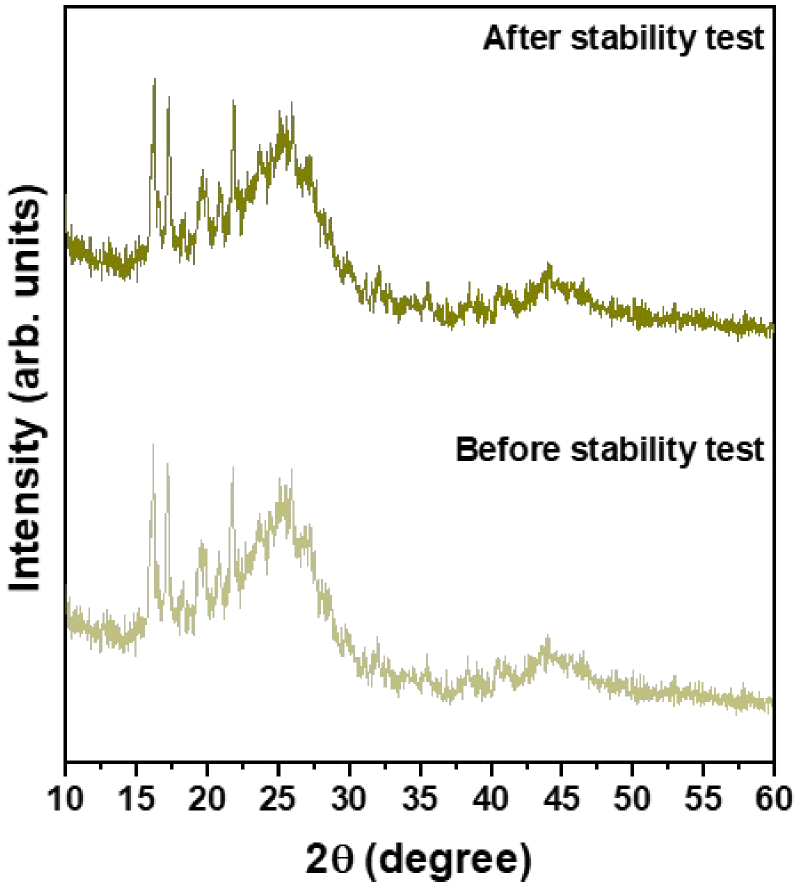

Fig. S20. XRD spectra of CuCoPBA-S catalyst electrode before and after the 10-hour stability test.

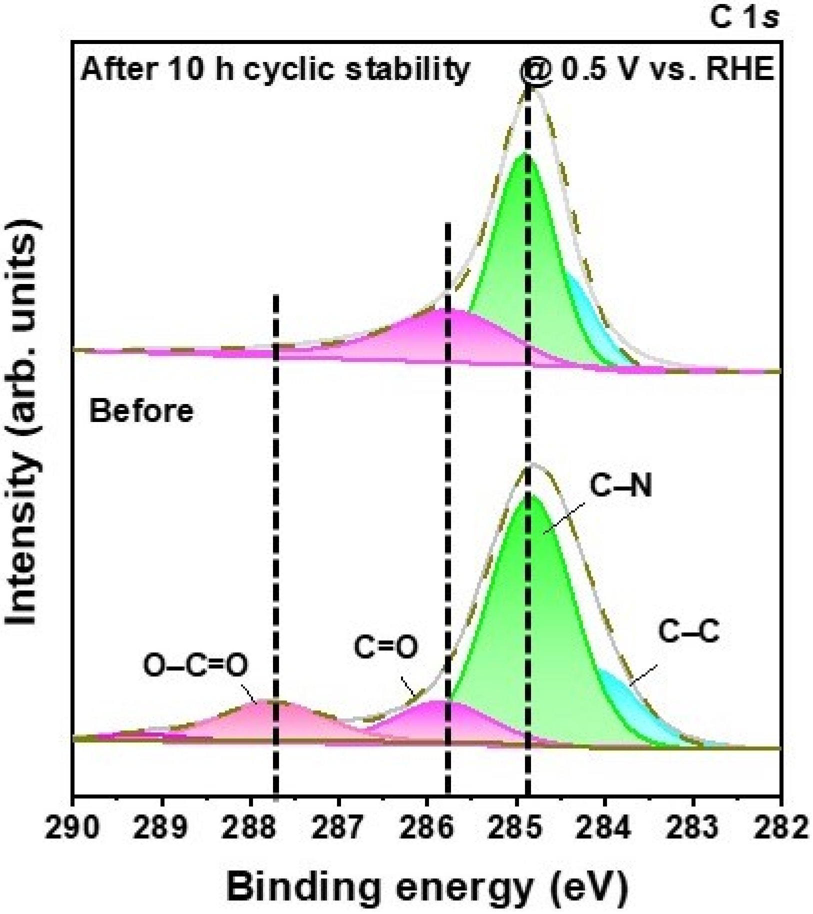

Fig. S21. XPS deconvoluted C 1*s* spectra of CuCoPBA-S catalyst electrode before and after the 10-hour stability test.

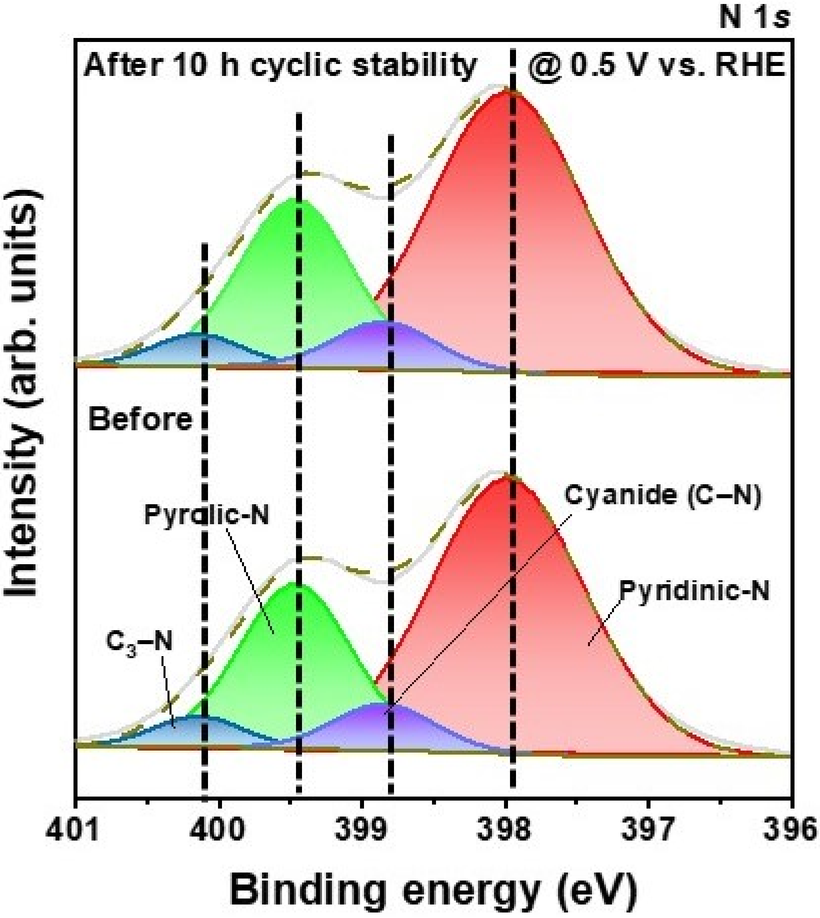

Fig. S22. XPS deconvoluted N 1*s* spectra of CuCoPBA-S catalyst electrode before and after the 10-hour stability test.

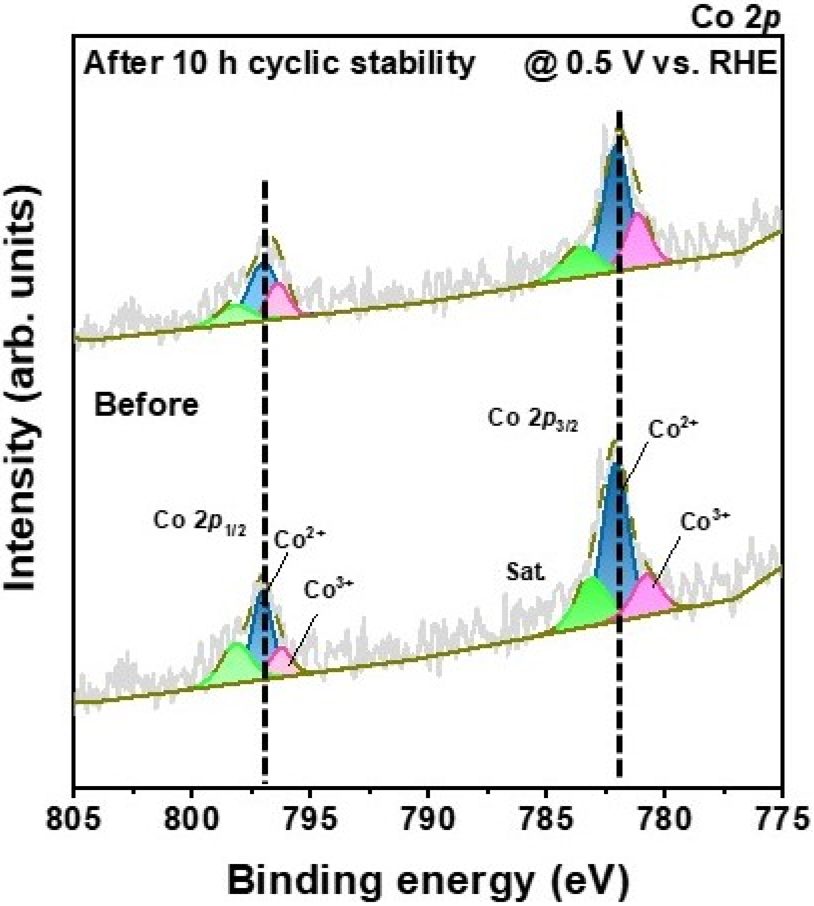

Fig. S23. XPS deconvoluted Co 2*p* spectra of CuCoPBA-S catalyst electrode before and after the 10-hour stability test.

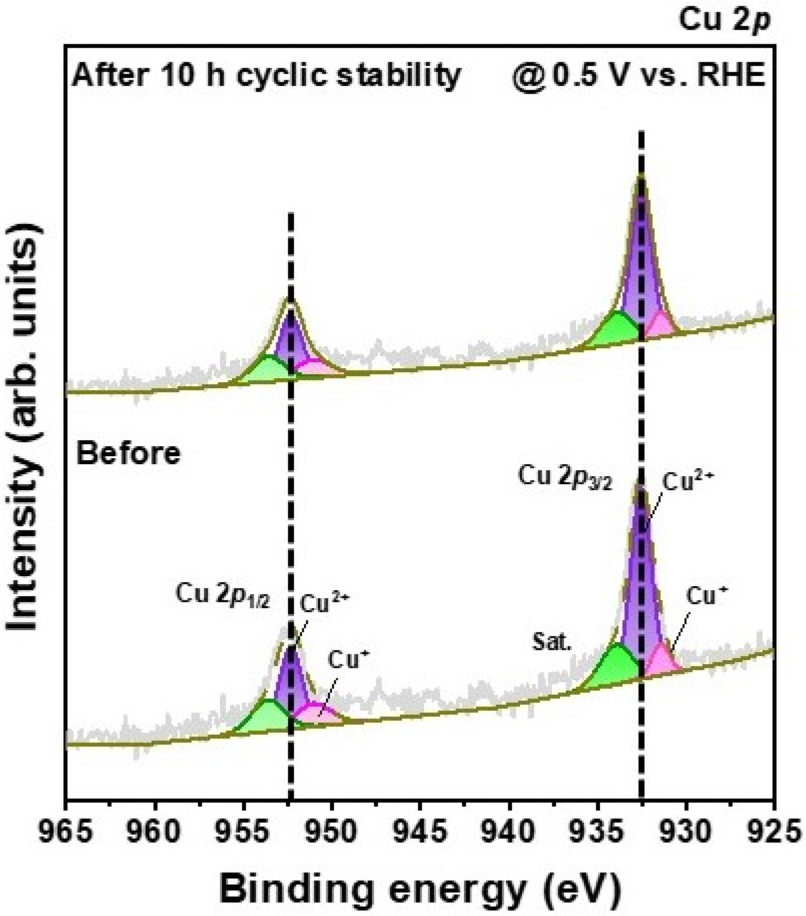

Fig. S24. XPS deconvoluted Cu 2*p* spectra of CuCoPBA-S catalyst electrode before and after the 10-hour stability test.

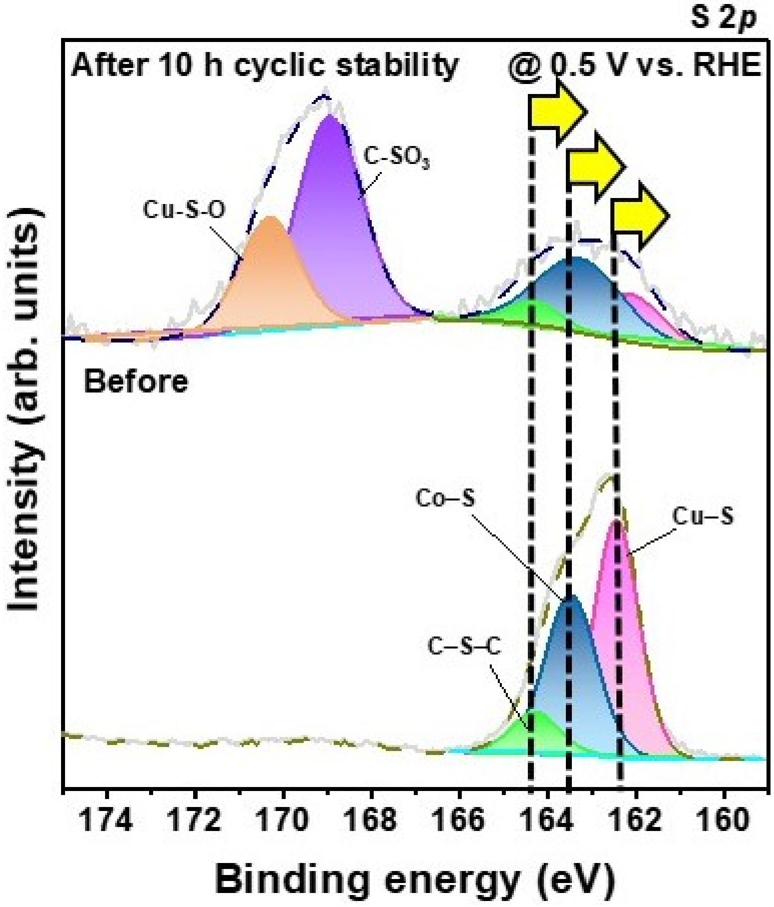

Fig. S25. XPS deconvoluted S 2*p* spectra of CuCoPBA-S catalyst electrode before and after the 10-hour stability test.

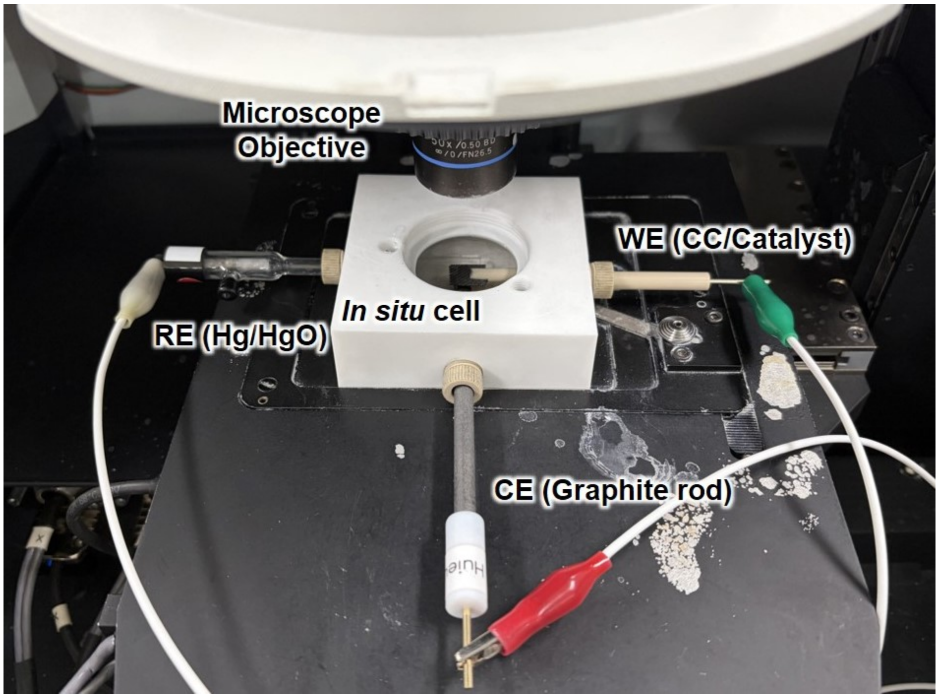

Fig. S26. Digital image of the experimental setup used for the *in situ* Raman spectroscopy measurement.

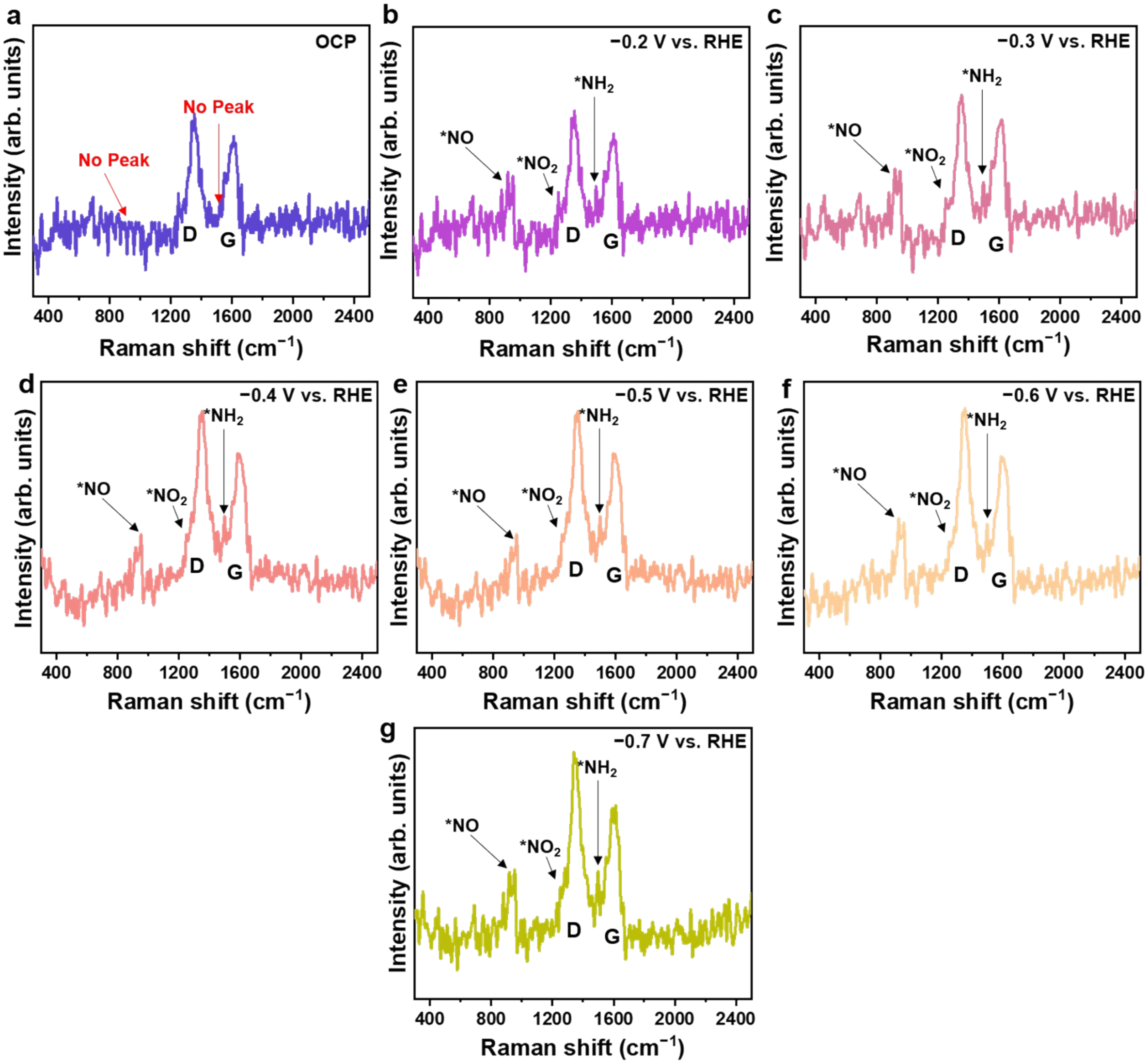

Fig. S27. In situ Raman spectra for CuCoPBA-S at different reduction potentials: (a) at OCP, (b) −0.2 V vs. RHE, (c) −0.3 V vs. RHE, (d) −0.4 V vs. RHE, (e) −0.5 V vs. RHE, (f) −0.6 V vs. RHE, and (g) −0.7 V vs. RHE.

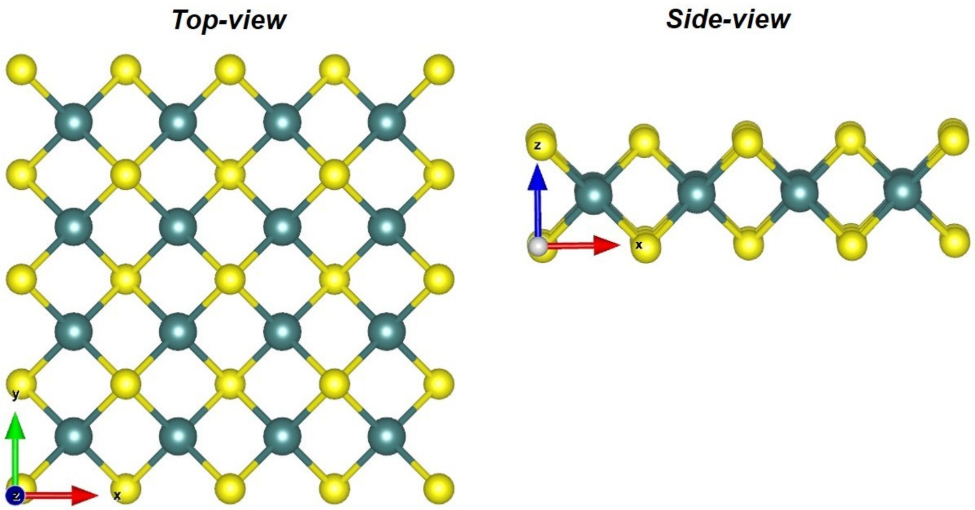

Top-view

Side-view

Fig. S28. DFT-optimized geometry for Cu_2S.

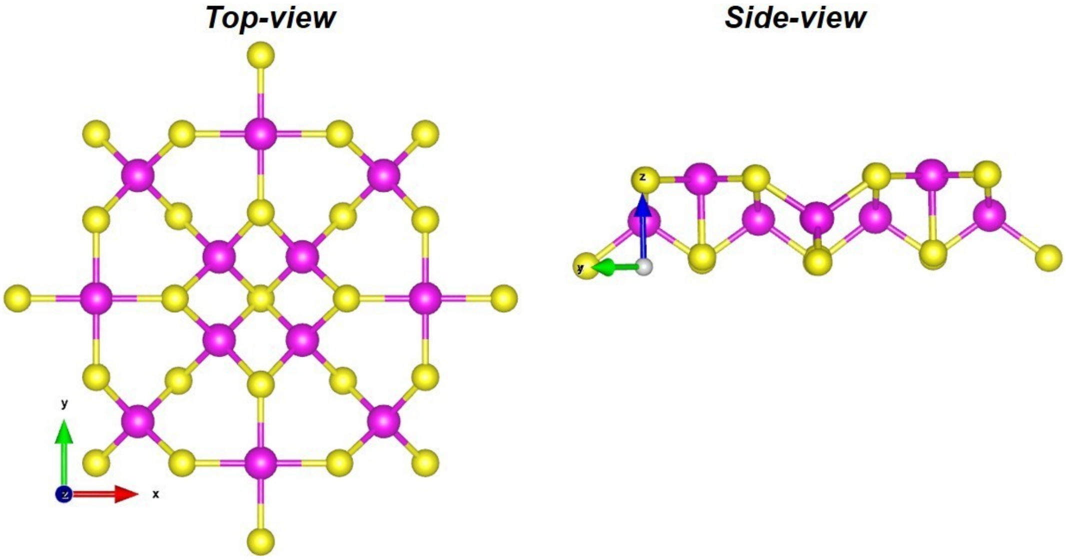

Fig. S29. DFT-optimized geometry for Co_9S_8.

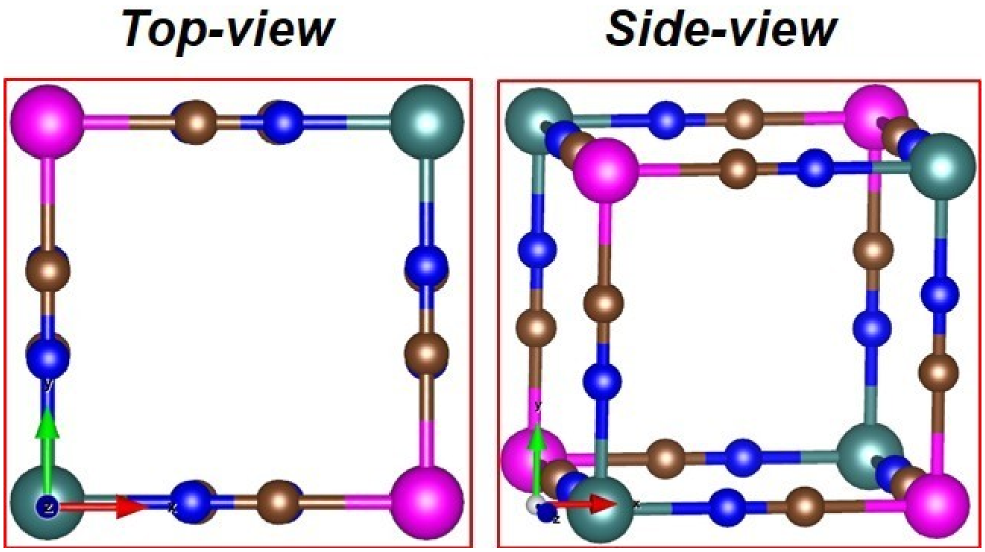

Fig. S30. DFT-optimized geometry for CoCuPBA.

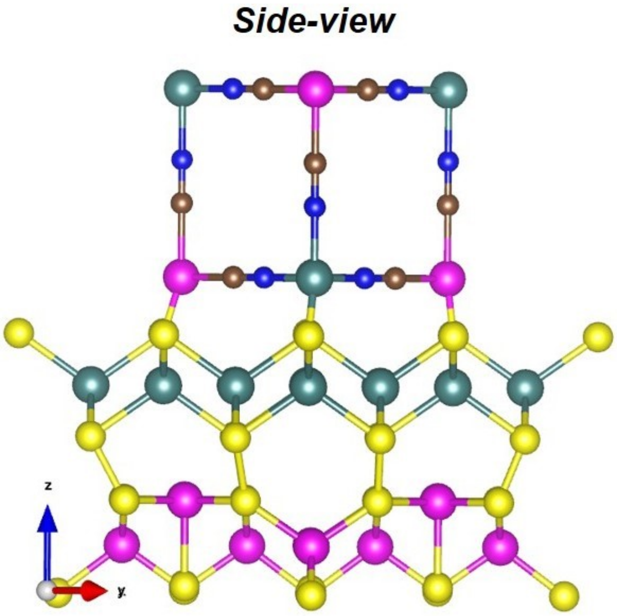

Fig. S31. DFT-optimized geometry for CoCuPBA-S.

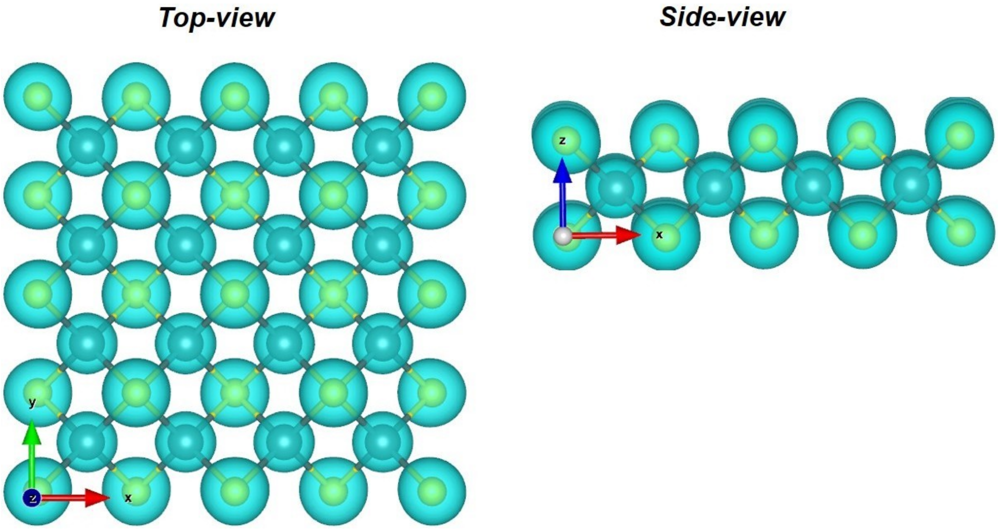
Top-view

Side-view

Fig. S32. DFT-optimized charge distribution in Cu_2S.

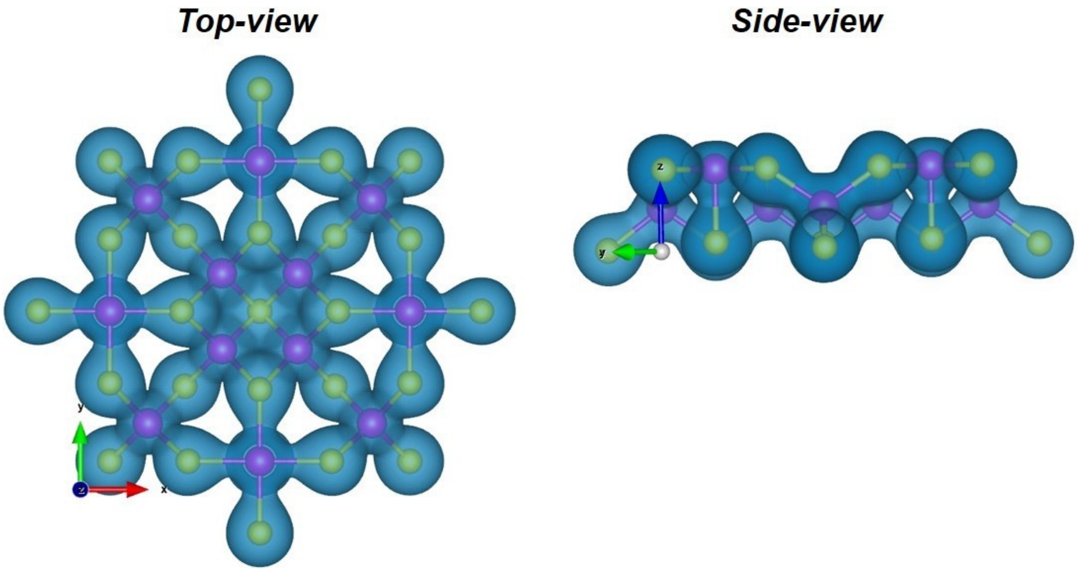

Top-view

Side-view

Fig. S33. DFT-optimized charge distribution in Co_9S_8.

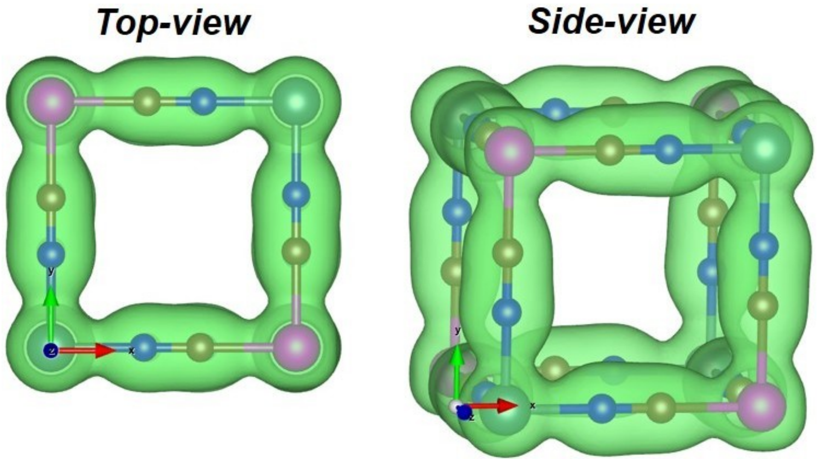

Fig. S34. DFT-optimized charge distribution in CuCoPBA.

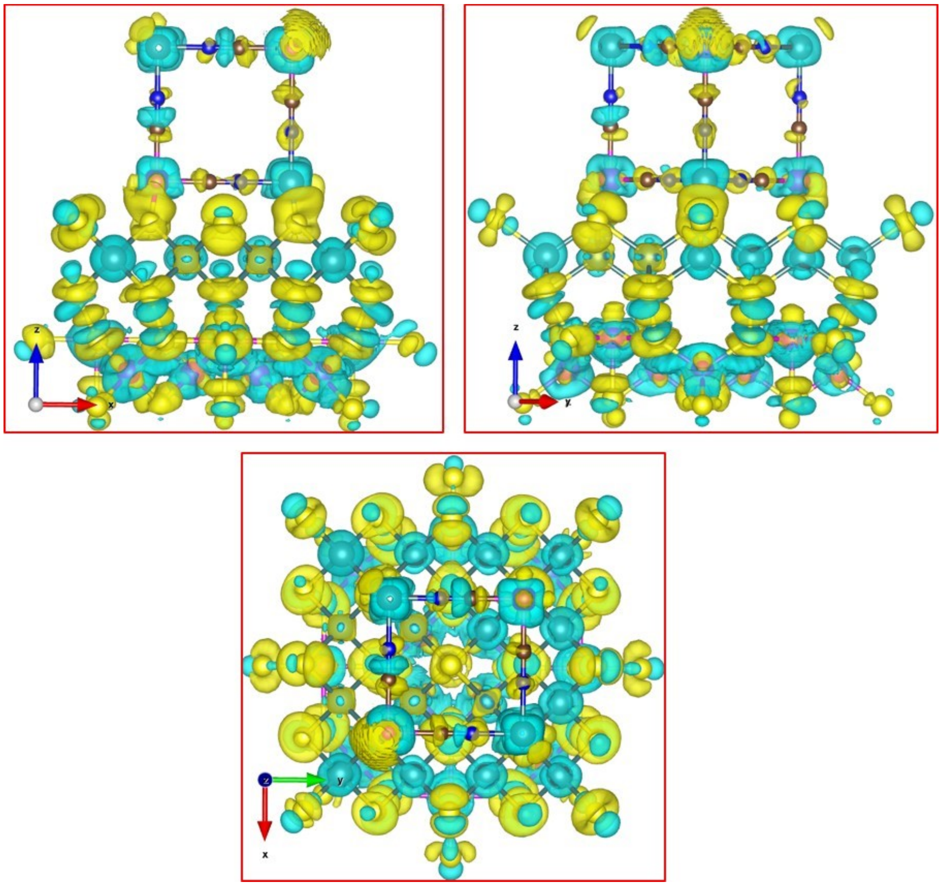

Fig. S35. DFT-optimized charge density difference covers the CuCoPBA surface.

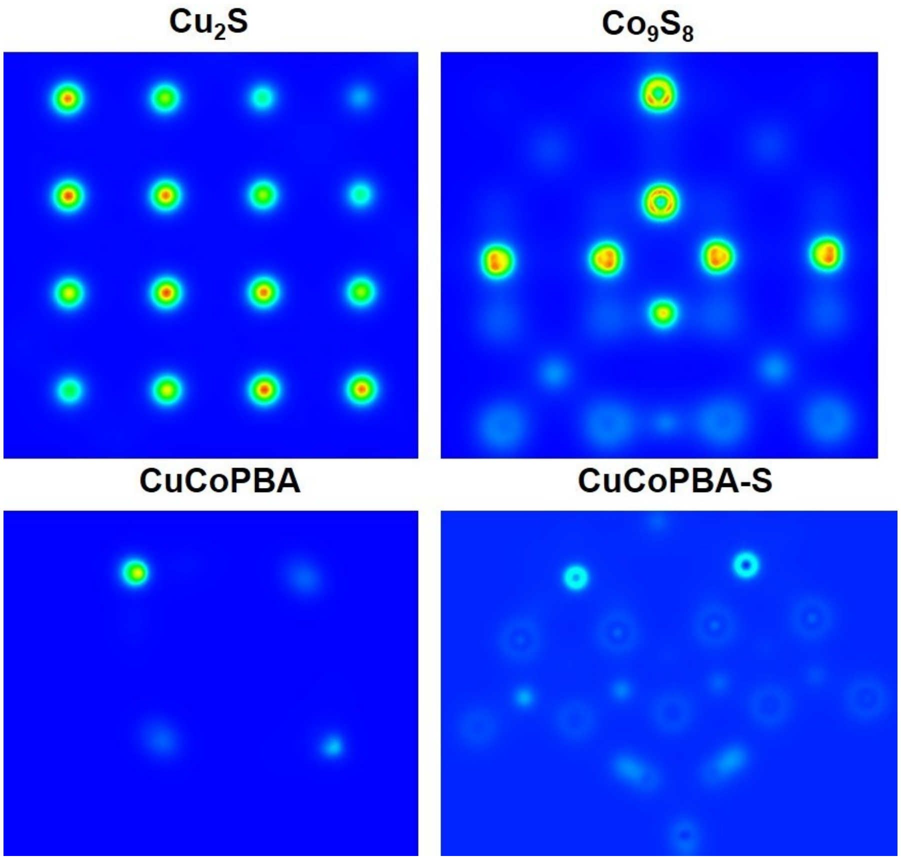

Fig. S36. DFT-optimized electron valence function (ELF) profile in Cu_2S, Co_9S_8, CuCoPBA, and CuCoPBA-S.

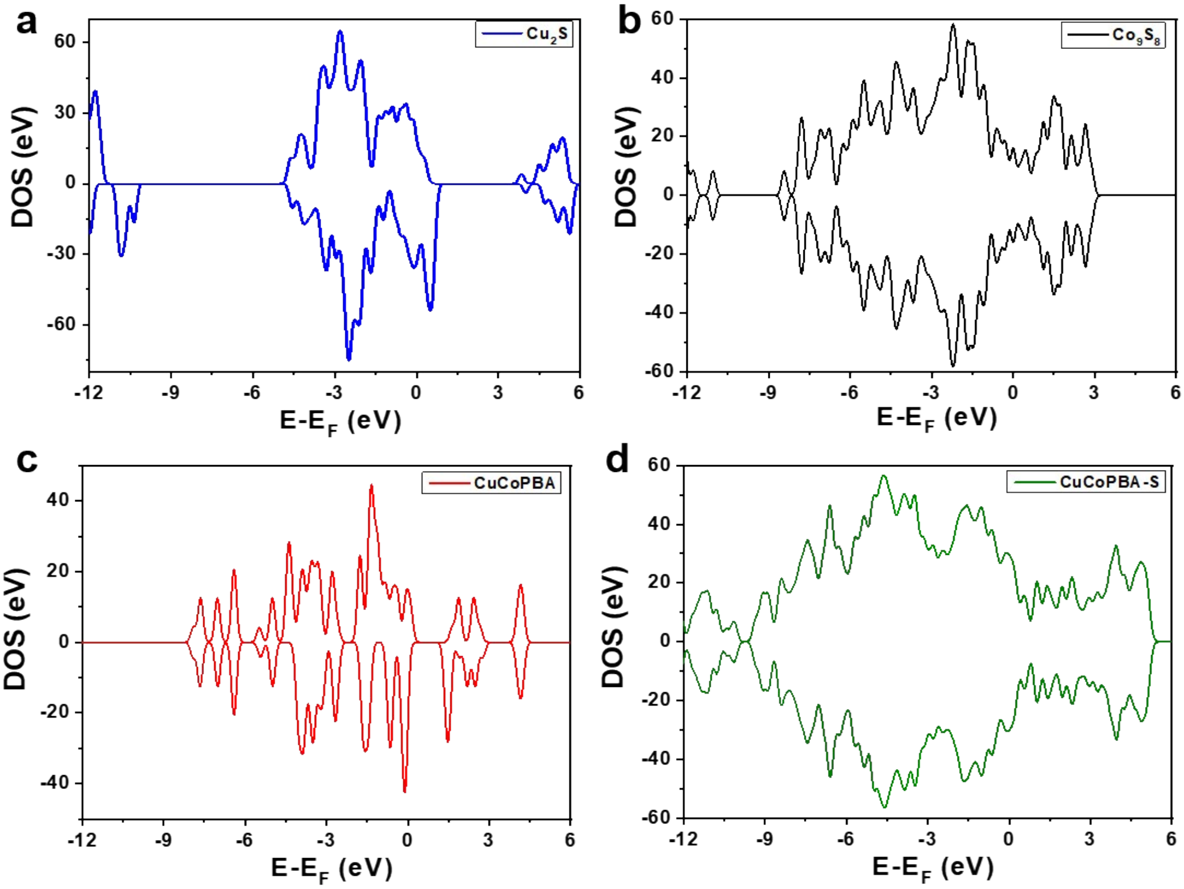

Fig. S37. DFT-calculated density of states of (a) Cu_2S, (b) Co_9S_8, (c) CuCoPBA, and (d) CuCoPBA-S.

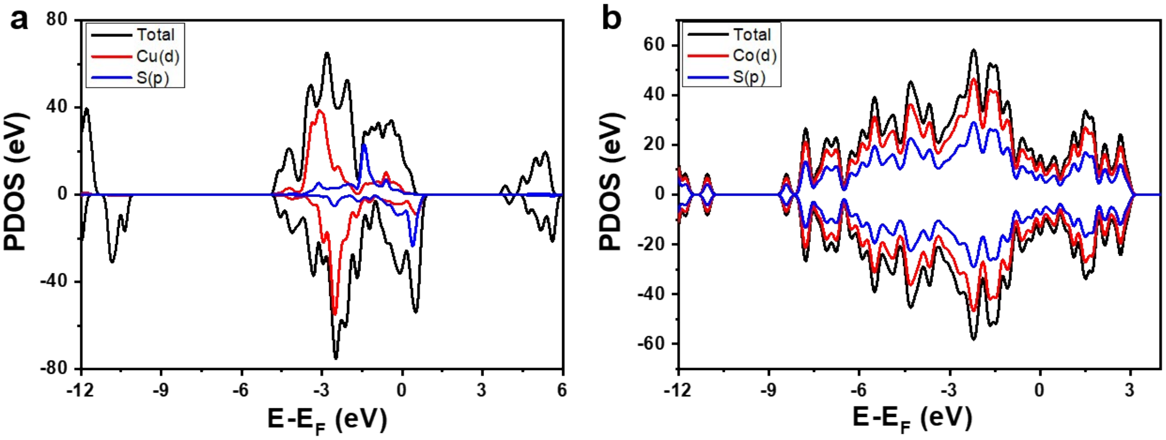

Fig. S38. DFT-calculated partial density of states (PDOS) for (a) Cu_2S and (b) Co_9S_8.

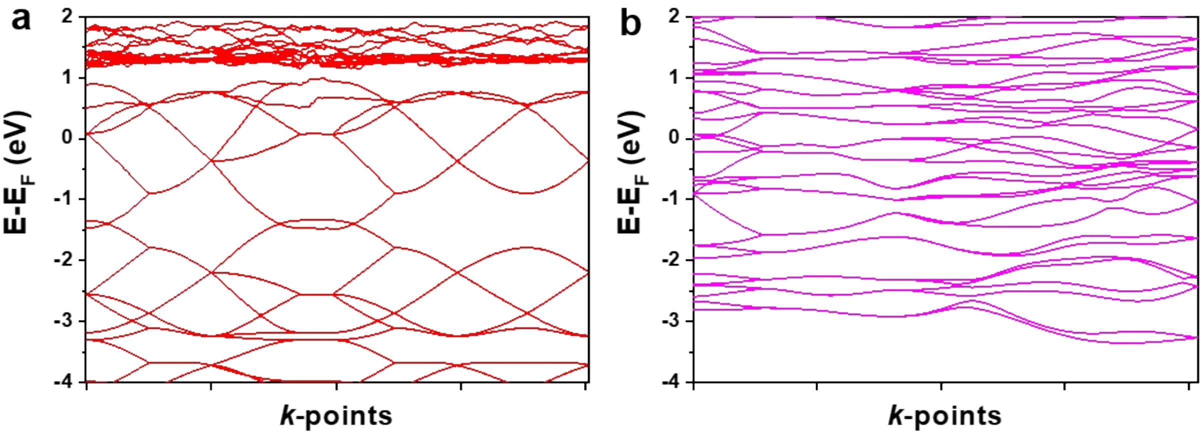

Fig. S39. DFT-computed band structure for (a) Cu_2S and (b) Co_9S_8.

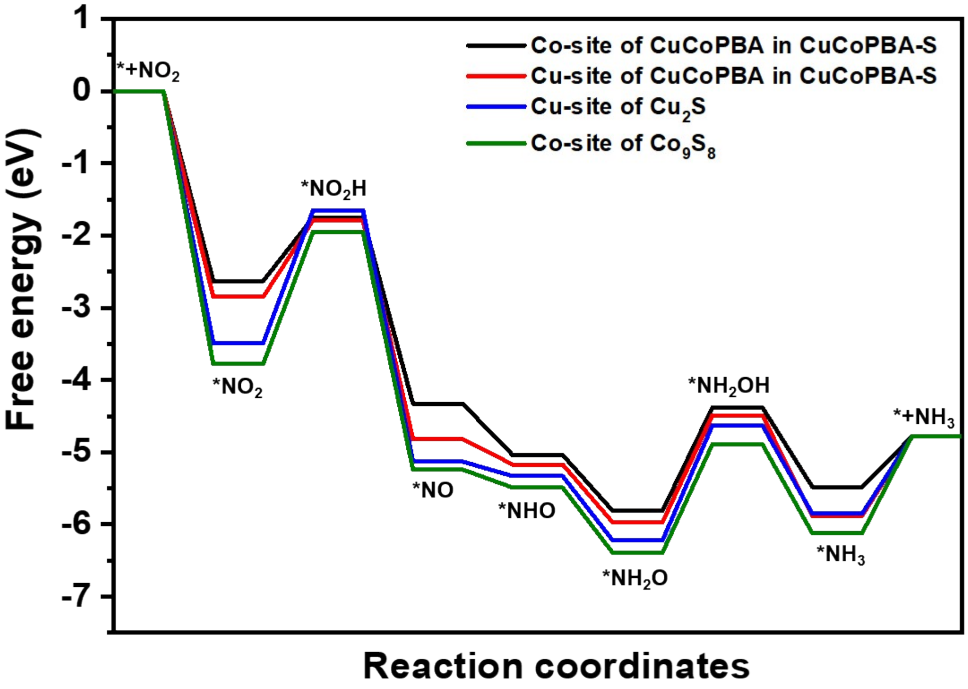

Fig. S40. The eNO_2RR free energy diagram over the Cu-site of CuCoPBA in CoCuPBA-S, Cu_2S and Co-site of CuCoPBA in CoCuPBA-S, Co_9S_8.

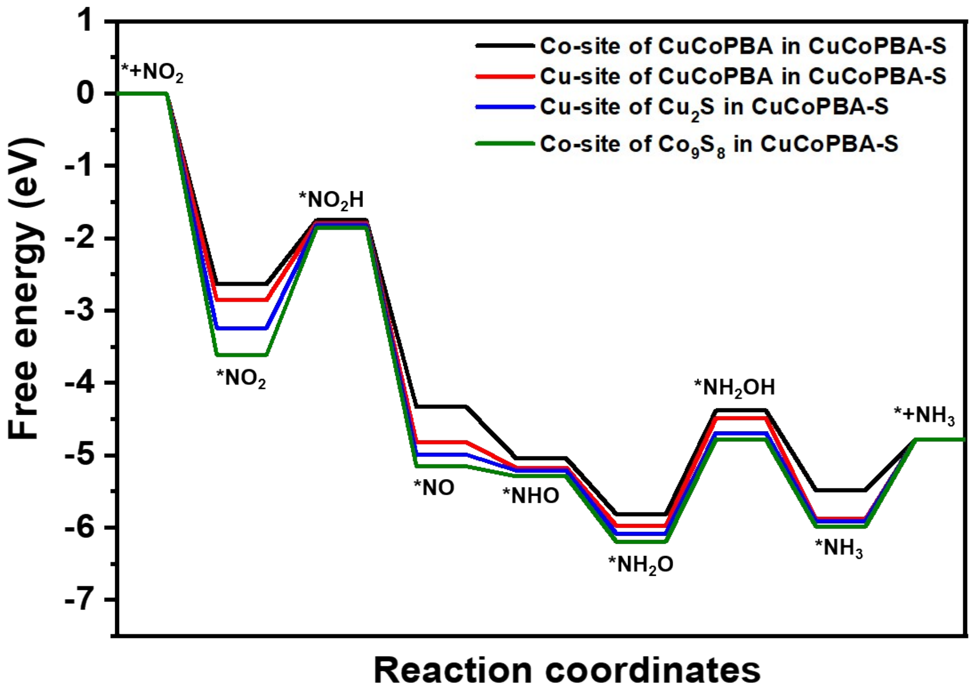

Fig. S41. The eNO$_2$RR free energy diagram over the Cu-site of CuCoPBA in CoCuPBA/Cu$_2$S/Co$_9$S$_8$, Cu$_2$S in CoCuPBA/Cu$_2$S/Co$_9$S$_8$, and Co-site of CuCoPBA in CoCuPBA/Cu$_2$S/Co$_9$S$_8$, Co-site of Co$_9$S$_8$ in CoCuPBA/Cu$_2$S/Co$_9$S$_8$.

Table S1. Parameters used in the XRD Rietveld measurement and the detailed phase analysis results.

R-Values
Rexp : 5.48 Rwp : 6.55 Rp : 5.15 GOF : 1.20
Rexp`: 25.42 Rwp`: 30.41 Rp` : 37.58 DW : 1.46

Quantitative Analysis - Rietveld		
Phase 1	CuSCN	7.5(18) %
Phase 2	Cobaltpentlandite	2.8(13) %
Phase 3	Cu_2S	48(5) %
Phase 4	S	10(2) %
Phase 5	$Cu_3[Co(CN)_6]_2$	32(4) %

Background	
One on X	1(1600)
Chebychev polynomial, Coefficient 0	260(60)
1	-20(50)
2	-70(30)
3	11(12)
4	1(6)
5	4(3)
6	9.1(13)
Instrument	
Primary radius (mm)	141.5
Secondary radius (mm)	141.5
Linear PSD 2Th angular range (°)	5
FDS angle (°)	1
Full Axial Convolution	
Filament length (mm) 12	12
Sample length (mm) 15	15
Receiving Slit length (mm) 12	12
Primary Sollers (°) 2.5	2.5
Secondary Sollers (°) 2.5	2.5

Corrections	
Zero error	0.131 (7)
LP Factor	0
Miscellaneous	
X Calculation Step	0.02

Structure 1	
Phase name	CuSCN
R-Bragg	3.508
Spacegroup	Pbca
Scale	0.0000012(3)
Cell Mass	973.027
Cell Volume (Å^3)	527.5(5)
Wt% - Rietveld	7.5(18)
Double-Voigt|Approach	
Cry size Lorentzian	600(1200)
k: 1 LVol-IB (nm)	400(800)
k: 0.89 LVol-FWHM (nm)	500(1100)
Crystal Linear Absorption Coeff. (1/cm)	161.83(17)
Crystal Density (g/cm^3)	3.063(3)
Lattice Parameters	
a (Å)	10.983(7)
b (Å)	7.195(5)
c (Å)	6.676(4)

Site	Np	x	y	z	Atom	Occ	Beq
Cu1	8	0.18428	0.15640	0.13598	Cu	1	0
S1	8	0.78357	0.38390	0.17407	S	1	0
C1	8	0.92453	0.29429	0.13920	C	1	0
N1	8	0.01656	0.23210	0.11760	N	1	0

Structure 2	
Phase name	Cobaltpentlandite
R-Bragg	1.838
Spacegroup	Fm-3m
Scale	0.00000008(3)
Cell Mass	3147.675
Cell Volume (Å^3)	985(2)
Wt% - Rietveld	2.8(13)
Double-Voigt|Approach	
Cry size Lorentzian	120(170)
k: 1 LVol-IB (nm)	80(110)
k: 0.89 LVol-FWHM (nm)	110(150)
Crystal Linear Absorption Coeff. (1/cm)	1307(3)
Crystal Density (g/cm^3)	5.306(11)
Lattice Parameters	
a (Å)	9.950(7)

Site	Np	x	y	z	Atom	Occ	Beg
Co1	4	0.50000	0.50000	0.50000	Co	1	1
Co2	32	0.12500	0.12500	0.12500	Co	1	1
S1	8	0.25000	0.25000	0.25000	S	1	1
S2	24	0.25000	0.00000	0.00000	S	1	1

Structure 3	
Phase name	Cu_2S
R-Bragg	0.589
Spacegroup	Fm-3m
Scale	0.000037(7)
Cell Mass	637.136
Cell Volume (Å^3)	173.1(5)
Wt% - Rietveld	48(5)
Double-Voigt|Approach	
Cry size Lorentzian	18(7)
k: 1 LVol-IB (nm)	12(4)
k: 0.89 LVol-FWHM (nm)	16(6)
Crystal Linear Absorption Coeff. (1/cm)	366.8(11)
Crystal Density (g/cm^3)	6.112(18)
Lattice Parameters	
a (Å)	5.573(6)

Site	Np	x	y	z	Atom	Occ	Beg
Cu2	4	0.50000	0.50000	0.50000	Cu	0.095	0
Cu3	192	0.10670	0.16600	0.28260	Cu	0.029	0
S1	4	0.00000	0.00000	0.00000	S	1	0
Cu1	8	0.25000	0.25000	0.25000	Cu	0.2575	0

Structure 4	
Phase name	S
R-Bragg	2.644
Spacegroup	Fddd:2
Scale	0.000000060(15)
Cell Mass	4104.320
Cell Volume (Å^3)	3240(4)
Wt% - Rietveld	10(2)
Double-Voigt|Approach	
Cry size Lorentzian	600(1300)
k: 1 LVol-IB (nm)	400(800)
k: 0.89 LVol-FWHM (nm)	500(1200)
Crystal Linear Absorption Coeff. (1/cm)	195.8(3)
Crystal Density (g/cm^3)	2.104(3)

Lattice Parameters	
a (Å)	10.417(7)
b (Å)	12.809(10)
c (Å)	24.28(2)

Site	Np	x	y	z	Atom	Occ	Beg
S1	32	0.03531	0.09156	0.37963	S	1	0
S2	32	0.03421	-0.03206	0.32599	S	1	0
S3	32	0.10583	0.04636	0.20070	S	1	0
S4	32	-0.04388	0.01895	0.25366	S	1	0

Structure 5	
Phase name	$Cu_3[Co(CN)_6]_2$
R-Bragg	1.482
Spacegroup	F-43m
Scale	0.0000051(6)
Cell Mass	620.713
Cell Volume (Å^3)	840(3)
Wt% - Rietveld	32(4)
Double-Voigt|Approach	
Cry size Lorentzian	22(4)
k: 1 LVol-IB (nm)	14(3)
k: 0.89 LVol-FWHM (nm)	20(4)
Crystal Linear Absorption Coeff. (1/cm)	97.9(3)
Crystal Density (g/cm^3)	1.227(4)
Lattice Parameters	
a (Å)	9.436(10)

Site	Np	x	y	z	Atom	Occ	Beg
Cu1	4	0.50000	0.00000	0.00000	Cu	0.75	0
N1	24	0.30300	0.00000	0.00000	N	0.5	0
C1	24	0.18900	0.00000	0.00000	C	0.5	0
Co1	4	0.00000	0.00000	0.00000	Co	0.5	0

Table S2. Comparison of the eNO_2RR performance of the CuCoPBA-S with different electrocatalysts reported in the literature.

Sl No.	Catalyst	Electrolyte	NH_3 yield rate	Reduction Potential (V) vs. RHE	Ref.
1	Ag nanoarray	0.1 M NaOH + 0.1 M NO_2^-	5751 µg h^{-1} cm^{-2}	−0.7	1
2	Pd/CuO	0.1 M K_2SO_4 + 0.01 M KNO_2	906.4 µg h^{-1} cm^{-2}	−0.84	2
3	Co@JDC	0.1 M NaOH + 0.1 M NO_2^-	2.8 ± 0.1 mol h^{-1} g^{-1}	−1.0	3
4	Ni@JBC-800	0.1 M NaOH + 0.1 M NO_2^-	4117.3 µg h^{-1} cm^{-2}	−0.5	4
5	Ni@MDC	0.1 M NaOH + 0.1 M NO_2^-	6300 µg h^{-1} cm^{-2}	−0.8	5
6	Ni@TiO_2	0.1 M NaOH + 0.1 M NO_2^-	568.7 µmol h^{-1} cm^{-2}	−0.5	6
7	Cu@TiO_2/TP	0.1 M Na_2SO_4 + 0.1 M NO_2^-	760.5 µmol h^{-1} cm^{-2}	−0.8	7
8	Ni-NSA-V_{Ni}	0.2 M Na_2SO_4 + 200 ppm NO_2^-	235.98 µmol h^{-1} cm^{-2}	−0.54	8
9	Ni-TiO_2	0.1 M NaOH + 0.1 M NO_2^-	380.27 µmol h^{-1} cm^{-2}	−0.5	9
10	V-TiO_2	0.1 M NaOH + 0.1 M NO_2^-	540.8 µmol h^{-1} cm^{-2}	−0.7	10
11	P-TiO_2	0.1 M Na_2SO_4 + 0.1 M NO_2^-	560.8 µmol h^{-1} cm^{-2}	−0.6	11
12	Cu_3P	0.1 M PBS + 0.1 M $NaNO_2$	1626.6 ± 36.1 µg h^{-1} cm^{-2}	−0.5	12
13	CoB	0.1 M Na_2SO_4 + 400 ppm NO_2^-	233.1 µmol h^{-1} cm^{-2}	−0.7	13
14	CoP	0.1 M PBS + 500 ppm NO_2^-	2260.7 ± 51.5 µg h^{-1} cm^{-2}	−0.2	14
15	Ni_2P	0.1 M PBS + 200 ppm NO_2^-	2692.2 µg h^{-1} cm^{-2}	−0.3	15
16	NiS_2@TiO_2	0.1 M NaOH + 0.1 M NO_2^-	591.9 µmol h^{-1} cm^{-2}	−0.6	16
17	**CuCoPBA-S**	**1 M KOH + 0.1 M KNO_2**	**3394.1 µg h^{-1} cm^{-2}**	**–0.5**	**This Work**

References

1. Q. Liu, G. Wen, D. Zhao, L. Xie, S. Sun, L. Zhang, Y. Luo, A. A. Alshehri, M. S. Hamdy and Q. Kong, Nitrite reduction over Ag nanoarray electrocatalyst for ammonia synthesis, *Journal of Colloid and Interface Science*, 2022, **623**, 513-519.
2. S. Liu, L. Cui, S. Yin, H. Ren, Z. Wang, Y. Xu, X. Li, L. Wang and H. Wang, Heterointerface-triggered electronic structure reformation: Pd/CuO nano-olives motivate nitrite electroreduction to ammonia, *Applied Catalysis B: Environmental*, 2022, **319**, 121876.
3. J. Wang, J. Liang, P. Liu, Z. Yan, L. Cui, L. Yue, L. Zhang, Y. Ren, T. Li and Y. Luo, Biomass Juncus derived carbon decorated with cobalt nanoparticles enables high-efficiency ammonia electrosynthesis by nitrite reduction, *Journal of Materials Chemistry A*, 2022, **10**, 2842-2848.
4. X. Li, Z. Li, L. Zhang, D. Zhao, J. Li, S. Sun, L. Xie, Q. Liu, A. A. Alshehri and Y. Luo, Ni nanoparticle-decorated biomass carbon for efficient electrocatalytic nitrite reduction to ammonia, *Nanoscale*, 2022, **14**, 13073-13077.
5. X. He, X. Li, X. Fan, J. Li, D. Zhao, L. Zhang, S. Sun, Y. Luo, D. Zheng and L. Xie, Ambient electroreduction of nitrite to ammonia over Ni nanoparticle supported on molasses-derived carbon sheets, *ACS Applied Nano Materials*, 2022, **5**, 14246-14250.
6. X. Ji, C. Ma, F. Zhang, X. He, X. Fan, J. Li, Z. Li, L. Ouyang, L. Zhang and T. Li, Ni@ TiO_2 nanoarray with the Schottky junction for the highly selective electrochemical reduction of nitrite to ammonia, *ACS Sustainable Chemistry & Engineering*, 2023, **11**, 2686-2691.

7. L. Ouyang, X. Fan, Z. Li, X. He, S. Sun, Z. Cai, Y. Luo, D. Zheng, B. Ying and J. Zhang, High-efficiency electroreduction of nitrite to ammonia on a Cu@TiO_2 nanobelt array, *Chemical Communications*, 2023, **59**, 1625-1628.
8. C. Wang, W. Zhou, Z. Sun, Y. Wang, B. Zhang and Y. Yu, Integrated selective nitrite reduction to ammonia with tetrahydroisoquinoline semi-dehydrogenation over a vacancy-rich Ni bifunctional electrode, *Journal of Materials Chemistry A*, 2021, **9**, 239-243.
9. Z. Cai, C. Ma, D. Zhao, X. Fan, R. Li, L. Zhang, J. Li, X. He, Y. Luo and D. Zheng, Ni doping enabled improvement in electrocatalytic nitrite-to-ammonia conversion over TiO_2 nanoribbon, *Materials Today Energy*, 2023, **31**, 101220.
10. H. Wang, F. Zhang, M. Jin, D. Zhao, X. Fan, Z. Li, Y. Luo, D. Zheng, T. Li and Y. Wang, V-doped TiO_2 nanobelt array for high-efficiency electrocatalytic nitrite reduction to ammonia, *Materials Today Physics*, 2023, **30**, 100944.
11. L. Ouyang, X. He, S. Sun, Y. Luo, D. Zheng, J. Chen, Y. Li, Y. Lin, Q. Liu and A. M. Asiri, Enhanced electrocatalytic nitrite reduction to ammonia over P-doped TiO_2 nanobelt array, *Journal of Materials Chemistry A*, 2022, **10**, 23494-23498.
12. J. Liang, B. Deng, Q. Liu, G. Wen, Q. Liu, T. Li, Y. Luo, A. A. Alshehri, K. A. Alzahrani and D. Ma, High-efficiency electrochemical nitrite reduction to ammonium using a Cu_3P nanowire array under ambient conditions, *Green Chemistry*, 2021, **23**, 5487-5493.
13. L. Hu, D. Zhao, C. Liu, Y. Liang, D. Zheng, S. Sun, Q. Li, Q. Liu, Y. Luo and Y. Liao, Amorphous CoB nanoarray as a high-efficiency electrocatalyst for nitrite reduction to ammonia, *Inorganic Chemistry Frontiers*, 2022, **9**, 6075-6079.

14. G. Wen, J. Liang, Q. Liu, T. Li, X. An, F. Zhang, A. A. Alshehri, K. A. Alzahrani, Y. Luo and Q. Kong, Ambient ammonia production via electrocatalytic nitrite reduction catalyzed by a CoP nanoarray, *Nano Research*, 2022, **15**, 972-977.
15. G. Wen, J. Liang, L. Zhang, T. Li, Q. Liu, X. An, X. Shi, Y. Liu, S. Gao and A. M. Asiri, Ni_2P nanosheet array for high-efficiency electrohydrogenation of nitrite to ammonia at ambient conditions, *Journal of Colloid and Interface Science*, 2022, **606**, 1055-1063.
16. X. He, L. Hu, L. Xie, Z. Li, J. Chen, X. Li, J. Li, L. Zhang, X. Fang and D. Zheng, Ambient ammonia synthesis via nitrite electroreduction over NiS_2 nanoparticles-decorated TiO_2 nanoribbon array, *Journal of Colloid and Interface Science*, 2023, **634**, 86-92.